SIMS Microanalysis of the Strelley Pool Formation Cherts and the Implications for the Secular-Temporal Oxygen-isotope Trend of Cherts

J.N. Cammack[1,6,7], M.J. Spicuzza[1,6], A.J. Cavosie[1,5], M.J. Van Kranendonk[2], A.H. Hickman[3], R. Kozdon[1,4,6], I.J. Orland[6], K. Kitajima[1,6], J.W. Valley[1,6]

[1]NASA Astrobiology Institute, Dept. of Geoscience, University of Wisconsin, 1215 W. Dayton St., Madison, WI, 53706, USA (valley@geology.wisc.edu or cammack88@gmail.com).
[2]Australian Centre for Astrobiology, and School of Biological, Earth and Environmental Sciences, University of New South Wales, Kensington, NSW 2052, Australia.
[3]Geological Survey of Western Australia, 100 Plain Street, Perth, WA 6004, Australia.
[4]Lamont-Doherty Earth Observatory of Columbia University, 61 Route 9W, Palisades, NY 10964, USA.
[5]Curtin University of Technology, GPO Box U1987 Perth, WA 6845, Australia.
[6] WiscSIMS, Depth of Geoscience, University of Wisconsin, 1215 W. Dayton St., Madison, WI, 53706, USA.
[7]Fort Lewis College, 1000 Rim Drive, Durango, CO, 81301, USA (jncammack@fortlewis.edu)

To be submitted to Precambrian Research

October 6, 2017

Abstract

The significance of oxygen isotope ratios in Archean chert has long been debated. Cherts from the c. 3.4 Ga Strelley Pool Formation (SPF) (Pilbara Craton, Western Australia) host some of the oldest stromatolite and microfossil evidence for life, but the genesis and timing of silica cements has been unclear. Field relations, petrography and a combination of laser fluorination and in-situ SIMS measurements of $\delta^{18}O$ in quartz show that bedded cherts of the SPF were originally precipitated as carbonates and were later widely replaced by quartz. Three localities were studied and analyzed for $\delta^{18}O(Qz)$ in chert: 1) Camel Creek: foliated, metamorphosed, bedded cherts and meter-scale black chert veins; 2) Unconformity Ridge and ABDP8 drill core: stromatolitic and bedded chert overlying basal detrital quartz sandstone; and 3) the Trendall locality: "bedded" stromatolitic chert replacing original dolomite, low temperature hydrothermal quartz, and mm- to decimeter-scale chert-quartz veins. Laser fluorination (mm-scale) values of $\delta^{18}O(Qz)$ range from: 14.2 to 18.2‰ VSMOW at Camel Creek; 9.3 to 18.9‰ at Unconformity Ridge; and 13.7 to 25.7‰ at Trendall. Values of $\delta^{18}O(Qz)$ in cm to decimeter-scale hydrothermal chert veins cutting bedded carbonates at Trendall range from ca. 15 to 16‰, whereas "bedded cherts" are 17 to 26‰. These laser data include the highest $\delta^{18}O$ values reported for cherts in Paleoarchean sediments and are up to 4‰ higher than the upper limit of ~22‰ reported in other studies, in apparent contrast to the long-standing secular-temporal trend which shows such high $\delta^{18}O$ only in younger chert. However, analysis by laser fluorination at the 1-mm scale cannot resolve microtextures seen petrographically. In contrast, in-situ SIMS analyses can resolve petrographic microtextures and show $\delta^{18}O(Qz)$ at 10-μm scale have an even greater range of 7 to 31‰ in "bedded" cherts at the Trendall locality, up to 9‰ above the secular-temporal trend.

Textures observed optically at the Trendall locality were classified as: microquartz,

mesoquartz, chalcedony, megaquartz veins, and cavity megaquartz. SEM-CL imaging shows two generations of meso- and megaquartz; bright CL with well-developed growth zoning, and dark CL with massive or mottled texture. Microquartz is the earliest textural generation of quartz and has a maximum $\delta^{18}O(Qz)$ of ~ 22‰ by SIMS. Dark-CL mesoquartz has similar $\delta^{18}O$ to microquartz and is interpreted to also be early. Bright CL mesoquartz, which formed post-Archean, has even higher $\delta^{18}O$, up to 29‰. Vein megaquartz crosscuts most quartz generations and has a restricted range of $\delta^{18}O$, mostly from 16 to 19‰. Chalcedony pseudomorphs rhombic cavities and fractures, lines the edges of veins, and has similar $\delta^{18}O$ to veins (16 to 19‰). Late cavity megaquartz is bright and zoned by CL, grows into late open cavities, and has the highest $\delta^{18}O(Qz)$ values reported from the Pilbara, up to 31.3‰. Thus, the highest-$\delta^{18}O$ quartz cements at the Trendall locality are the youngest and may be related to weathering. Early silicification and the formation of microquartz, chalcedony and low $\delta^{18}O$ mesoquartz occurred during low temperature hydrothermal activity in the Archean.

None of the SPF quartz examined is interpreted to have formed as a direct precipitate from Paleoarchean seawater. Thus, values of $\delta^{18}O(Qz)$ do not record either water chemistry or temperature of Archean oceans. In-situ SIMS analysis shows that high-$\delta^{18}O(Qz)$ values above 22‰ are only found in late-forming cavity megaquartz and high $\delta^{18}O$ mesoquartz at the Trendall locality.

The SPF results from our sample suite demonstrate the ability to resolve complex history using detailed petrography and SIMS analysis. Similar studies may show equal complexity of $\delta^{18}O(Qz)$ data for other localities that are interpreted to show secular-temporal trends for chert. The apparent increase of $\delta^{18}O(Qz)$ through time may reflect differences in diagenesis, and/or an inherent and previously unrecognized sampling bias that compares fundamentally different populations of quartz, such as Archean hydrothermal chert from volcanic greenstone belts, with unrelated Phanerozoic biogenic quartz.

Keywords

Archean, chert, oxygen isotopes, Strelley Pool Formation, secular trends, SIMS, stromatolite

Introduction

Systematically lower oxygen isotope ratios in cherts with increasing age were one of the earliest observations of stable isotope geochemistry (Degens and Epstein, 1962) and have been reinforced by many subsequent studies (Knauth, 1992, 2005; Robert and Chaussidon, 2006; Perry and Lefticariu, 2007; Shields, 2007; Cunningham et al., 2012; Tartèse et al., 2017) (Figure 1). Similar secular-temporal oxygen isotope trends are observed for carbonates (Perry and Tan, 1972; Veizer and Hoefs, 1976; Veizer et al., 1999; Prokoph et al., 2008) and phosphates (Karhu and Epstein, 1986; Blake et al., 2010). Secular trends in oxygen isotope ratios have led to controversial conclusions that: Archean oceans were warmer (> 60^{o}C) than Phanerozoic oceans (Karhu and Epstein, 1986; Knauth, 2005; Robert and Chaussidon, 2006; Schwartzman et al., 2007; Tartèse et al., 2017); δ^{18}O of seawater was lower (Walker and Lohmann, 1989; Kasting et al., 2006; Jaffrés et al., 2007); or older cherts are more altered and do not retain their primary δ^{18}O (Degens and Epstein, 1962, 1964; Shields, 2007).

Most previous studies analyzed bulk samples at the mm-to-cm scale and were unable to resolve zoning or other petrographically defined variations with correlated oxygen isotope trends at the µm scale. Secondary ion mass spectrometry (SIMS) has allowed in-situ analysis of oxygen isotope ratios in quartz at the 10-µm scale (Hervig, 1992; Valley and Graham, 1996; Kelly et al., 2007; Valley and Kita, 2009). More recently, SIMS has been applied to cherts (Robert and Chaussidon, 2006; Marin et al., 2010; Marin-Carbonne et al., 2014). Low values of δ^{18}O(Qz) in

Figure 1 are typically interpreted to result from diagenetic alteration and exchange with meteoric or hydrothermal fluids (Perry and Tan, 1972; Knauth, 2005; Robert and Chaussidon, 2006), and elevated $\delta^{18}O(Qz)$ values have been accepted as the 'least altered' chert and most pristine record of seawater by these authors.

This study examines cherts in the ~ 3.4 Ga Strelley Pool Formation (SPF) of the Pilbara Craton, Western Australia using new SIMS $\delta^{18}O(Qz)$ data correlated to micro-textures in order to address questions of chert genesis and aid in interpreting the secular-temporal trend of $\delta^{18}O$ (Figure 1). No previous studies of the SPF have combined in-situ SIMS microanalysis of $\delta^{18}O$ with detailed petrography. Values of $\delta^{18}O(Qz)$ from the SPF are used to test three hypotheses that would explain a secular trend: elevated Archean seawater temperatures; changing $\delta^{18}O$ of seawater; or alteration of quartz. This project integrates regional, outcrop and mm- to µm-scale petrographic studies of SPF quartz textures in conjunction with SIMS and laser fluorination (LF) $\delta^{18}O$ measurements on quartz and cherts from bedded, stromatolitic, and detrital lithostratigraphic members of the Strelley Pool Formation (SPF). The $\delta^{18}O(Qz)$ data test petrographic and temporal relations that provide insight into the secular $\delta^{18}O$ trend of cherts. The primary goal is to determine which, if any, SPF quartz generations precipitated in thermal and isotopic equilibrium with Paleoarchean seawater.

Mechanisms Controlling $\delta^{18}O$ of Cherts

In this study, the term chert is used broadly to represent rocks that are >98 % monomineralic, chemically precipitated quartz (e.g., Folk, 1980). The $\delta^{18}O$ of quartz in chert is controlled by the temperature at which it precipitates, $\delta^{18}O$ of formation fluid, and any post-crystallization isotopic exchange. In a water-rich system where quartz is at isotopic equilibrium, increased temperature results in a smaller fractionation [$\Delta^{18}O(Qz\text{-}H_2O)$] and lower $\delta^{18}O(Qz)$

(Pollington et al., 2016) (Supplementary Figure 1). Phanerozoic and modern cherts often form diagenetically during burial. These cherts follow a reaction pathway starting with dissolution-precipitation of biogenic opal-A (siliceous ooze composed of radiolarian, diatoms and sponge spicules) to opal-CT (hydrous silica), and finally form fibrous chalcedony or microcrystalline quartz (Murata and Nakata, 1974; Keene, 1975; Riech and von Rad, 1979; Hein and Yeh, 1983; Williams and Crerar, 1985; Bohrmann et al., 1994; Knauth, 1994). During this sequence, exchange with diagenetic fluids typically causes the final crystalline quartz to have $\delta^{18}O$ values 6-10‰ lower than the original biogenic opal precursors (Knauth and Epstein, 1976; Matheney and Knauth, 1993; Behl and Garrison, 1994). However, if the concentration of silica in diagenetic fluids remains below the solubility of opal-CT (Kastner et al., 1977; Siever, 1992), then chert may form directly from opal-A.

The Secular-Temporal Trend of $\delta^{18}O$ Chert

Archean to Mesoproterozoic chert is inherently different from Phanerozoic cherts. There was no known biogenic silica fixation by organisms prior to the evolution of Ediacaran sponges at c. 543-549 Ma (Brasier et al., 1997; Wang et al., 2010). In the absence of biogenic silica fixation, marine silica concentrations may have exceeded 60 ppm (Siever, 1992), with the possibility of abiogenic silica precipitation under ambient seawater temperatures (Knauth, 1994; Gunnarsson and Arnórsson, 2000; Perry and Lefticariu, 2007).

Figure 1 shows the compiled values for $\delta^{18}O(Qz)$ in Precambrian to Phanerozoic chert (from Perry and Lefticariu, 2007). Cherts found in units of older depositional-age are lower in $\delta^{18}O$ and there is an apparent step up to higher values at the end of the Archean. Solid lines define the range of $\delta^{18}O(Qz)$. The black-dashed line represents the maximum chert $\delta^{18}O$ from Robert and Chaussidon (2006) and the grey dot-dash lines represent the range of carbonate $\delta^{18}O$

from Shields and Veizer (2002).

Ocean Temperature in the Archean

Many studies have interpreted chert $\delta^{18}O$ data as a paleoclimate proxy and estimated seawater temperatures in excess of 60° C during the Archean (Knauth and Lowe, 2003; Knauth, 2005; Robert and Chaussidon, 2006; Schwartzman et al., 2007; Tartèse et al., 2017). Temperature estimates assume that seawater $\delta^{18}O$ has remained relatively constant (ca. 0 ±1‰) throughout Earth's history, that quartz in chert is unaltered, and that processes of chert formation are comparable to modern environments. Knauth and Lowe (2003) report bulk $\delta^{18}O$(chert) data uniformly below 22‰ in 3.5 Ga metamorphosed bedded cherts from the Barberton Greenstone Belt in South Africa. They discussed a possible 6-10‰ reduction in $\delta^{18}O$ during diagenesis from opal to chert, but interpreted the highest $\delta^{18}O$(Qz) values as a paleotemperature proxy for Archean seawater, reasoning that some cherts that originally had $\delta^{18}O$ values above 22‰ were lowered in $\delta^{18}O$ by diagenesis. Karhu and Epstein (1986) analyzed $\delta^{18}O$ in phosphates that were interpreted to be co-precipitated with quartz in cherts and estimated seawater temperatures as high as 80°C. If waters are assumed to be marine, these results are interpreted to indicate little change in $\delta^{18}O$(seawater).

There are several lines of evidence that argue against uniformly hot Archean oceans. The upper temperature limit for chlorophototrophy is ~73°C (Brock and Brock, 1968; Boyd et al., 2010; Hamilton et al., 2012). If organisms responsible for forming stromatolites in the Archean and Paleoproterozoic included chlorophotoautrophs, which seems likely given their conical morphology and photic zone sedimentary facies (Hofmann et al., 1999; Allwood et al., 2007), temperatures should have been 60° C or less for these organisms to thrive (Hamilton et al., 2012). The Archean sun was ~70% as luminous as today, leading some to conclude that the Earth's oceans would have frozen in the absence of a very thick greenhouse atmosphere (Sagan and Mullen, 1972; Kasting, 1993). Glacial diamictites at ~2.9 Ga in the Kaapvaal Craton of South Africa (Young et al., 1998) were deposited at an estimated paleolatitude of 48° (Nhleko, 2003) and low paleolatitude (4-11°) glacial diamictite deposited at ~2.4 - 2.3 Ga in the Huronian Supergroup of Ontario (Williams and Schmidt, 1997) further argue against uniformly hotter Precambrian oceans. Blake et al. (2010) measured $\delta^{18}O$ of 16 to 20‰ for Paleoarchean phosphates and estimated temperatures from 26 to 35° C in surface seawater (assuming $\delta^{18}O$(water) = 0‰).

Seawater $\delta^{18}O$ in the Archean

Changes in the $\delta^{18}O$ of seawater are likewise controversial. Values of $\delta^{18}O$(seawater) as low as -12 ‰ VSMOW have been proposed for the Precambrian (Jaffrés et al., 2007). In contrast, modern seawater $\delta^{18}O$ is relatively consistent at ~ 0 ± 1‰ (Hoefs, 2015). Small, short-term changes in seawater $\delta^{18}O$ are caused by variations in the amount of meteoric water stored on the continents as ice during glacial (seawater $\delta^{18}O \approx +1$‰) or inter-glacial (≈ -1‰) periods (Jaffrés et al., 2007; Perry and Lefticariu, 2007). Seawater $\delta^{18}O$ might also vary due to changes in global water-rock interaction such as hydrothermal activity at mid-ocean ridges, which vary with seafloor spreading rates. Tartèse et al. (2017) measured $\delta^{18}O$ in organic matter from Precambrian cherts and concluded that $\delta^{18}O$(seawater) was 0 ± 5‰ throughout the Archean.

Rock altered by hydrothermal activity at mid-ocean ridges provides another line of evidence for seawater $\delta^{18}O$ trends. The modern $\delta^{18}O$ value of seawater (0‰) results from an average $\delta^{18}O$ of altered oceanic crust (~ 6‰) and an average $\Delta^{18}O$(rock-seawater) ~ 6‰ (Gregory, 1991). If seawater changed in $\delta^{18}O$, then the $\delta^{18}O$ of altered rocks would be affected.

However, $\delta^{18}O$ values of Archean pillow basalts from the Pilbara (~6 to 12‰, Gregory, 1991) are similar to those in Cenozoic ophiolites (Muehlenbachs, 1998). Based on mass-balance models, Gregory (1991) estimated that seawater remained at -1.3 ± 1‰ and Muehlenbachs (1998) estimated 0 ± 2‰ throughout Earth's plate tectonic history. Putative Archean eclogite with $\delta^{18}O$ values of 4.7 to 6.9‰ (Jacob, 2004) suggest subduction of oceanic basalt altered by seawater similar to today as early as 3 Ga (Jacob et al., 1994; Jacob, 2004; Shirey and Richardson, 2011).

Alteration of Archean Chert

It has also been proposed that older rocks (cherts, carbonates and phosphates) are more altered on average and thus have lower $\delta^{18}O$ (Degens and Epstein, 1962, 1964; Karhu and Epstein, 1986; Shields, 2007; Prokoph et al., 2008). However, the proposal that low $\delta^{18}O$ Archean cherts result largely from alteration has been challenged on the basis that carbonates would be more strongly affected by alteration than cherts and that phosphates would be less altered. Thus, these rocks/minerals should not have the similar ~10‰ secular trends that cherts show (Wenzel et al., 2000; Kasting et al., 2006).

In summary, none of these three interpretations adequately explains the secular trend of $\delta^{18}O(Qz)$ for cherts.

Geology of the Strelley Pool Formation

The Strelley Pool Formation (SPF) sedimentary rocks are a prominent regional stratigraphic marker that is recognized in 11 of the 20 greenstone belts throughout the East Pilbara Terrane in Western Australia (Figure 2) (Hickman, 2008). The SPF unconformably overlies the Warrawoona Group (Buick et al., 1995; Van Kranendonk, 2006) and conformably underlies the 3350 Ma Euro Basalt of the Kelly Group (Hickman, 2008; Wacey et al., 2010).

Conglomerates and sandstones of variable thickness mark the unconformity at the base of the SPF, which locally is subaerial and represents the oldest known angular unconformity on Earth (Buick et al., 1995). Breccias and conglomerates at the top of the SPF, derived from lower SPF members, indicate a second period of erosion prior to the deposition of the Euro Basalt (Hickman, 2008). Based on zircon geochronology from the Warrawoona (3530 to 3427 Ma) and Kelly (3350 to 3315 Ma) Groups, SPF deposition occurred after 3427 Ma and ceased before 3350 Ma (Nelson, 1998; Van Kranendonk et al., 2002; Van Kranendonk and Pirajno, 2004; Hickman, 2008; Wacey et al., 2010). SPF deposition thus represents a volcanically quiescent period of up to 75 Myr (Hickman, 2008).

The Strelley Pool Formation includes some of the oldest, low-grade cherts and offers unique opportunities to evaluate conditions on the early Earth. The first detailed study of the Strelley Pool Formation by Lowe (1983) interpreted portions of the SPF as silicified carbonate and evaporite deposits from a peritidal, partially-restricted marine environment and numerous studies have corroborated these interpretations. The SPF hosts unsilicified, partially-silicified, and completely silicified dolomitic stromatolites comprising spectacular macroscopic evidence for early life on Earth (Hofmann et al., 1999; Allwood et al., 2007). Several studies provide morphological and geochemical evidence for microfossils and biogenic kerogen preserved in microcrystalline quartz of the SPF (Wacey et al., 2011a; Lepot et al., 2013; Sugitani et al., 2013; Brasier et al., 2015; Duda et al., 2016). These structures are now generally accepted as strong evidence for life at ~ 3.4 Ga, although the stromatolitic forms were once interpreted as abiogenic (Lowe, 1994; Lindsay et al., 2005).

Strelley Pool Fm. Lithostratigraphy and Sample Localities

The SPF consists of three major lithostratigraphic members (Van Kranendonk, 2011).

Member 1 (M1) at the base is composed of coarse to medium-grained clastic units of sandstone and pebble to boulder conglomerate. Member 2 (M2) has bedded dolomite, stromatolitic dolomite, radiating crystal fans replaced by dolomite and largely silicified, and partly to completely silicified stromatolitic dolomite. Member 3 (M3) at the top is a coarse clastic unit chiefly composed of cobble to boulder conglomerates, coarse sandstones, and breccia. Anastomosing, decimeter- to meter-scale, grey to black hydrothermal veins that are primarily composed of black, very fine-grained quartz (chert) that cut across and parallel to bedding in all three members (Van Kranendonk, 2011:Figure 3 and Supplementary Figure 2). Veins are locally observed in the underlying Warrawoona Group and terminate within the SPF; veins do not cross up into the Euro Basalt overlying the SPF (Van Kranendonk et al., 2001; Van Kranendonk and Pirajno, 2004; Van Kranendonk, 2011). Smaller quartz veins (mm- to-μm scale) are observed in thin section to cut across chert textures.

Trendall Locality

The majority of SIMS $\delta^{18}O$ data in this study are from M2 of the Strelley Pool Formation, collected from the Trendall locality (Figures 2 and 3). This area (the Trendall Reserve) has been protected from unauthorized sampling since 2009 because it includes exceptional examples of coniform stromatolitic dolomite and chert (Hofmann et al., 1999; Hickman et al., 2011; Van Kranendonk, 2011). Samples analyzed here were collected from float prior to 2009.

The SPF at the Trendall locality is cut by decimeter- to meter wide, dark grey to black hydrothermal chert veins, which were analyzed for $\delta^{18}O(Qz)$ and compared to the M2 "bedded" cherts (silicified bedded dolomites: Figure 3 and Supplementary Figure 2). Data and interpretations from the Camel Creek locality and from the Unconformity Ridge locality are also reported for comparison to the Trendall locality, based on details presented in Cammack (2015).

Post-Depositional and Penecontemporaneous Processes

In this study, 'hydrothermal' is used broadly to describe circulating fluids that were warmer (i.e., 50°C to 350°C) than the rocks they interacted with. Many studies have documented geochemical and field evidence of hydrothermal activity and silicification in the SPF and other units of the Pilbara Supergroup (Buick et al., 1981; Lowe, 1983; Buick and Dunlop, 1990; Van Kranendonk et al., 2003; Van Kranendonk and Pirajno, 2004; Sugitani et al., 2006; Van Kranendonk, 2006; Hickman, 2008; Rouchon and Orberger, 2008; Wacey et al., 2010; Boorn et al., 2007, 2010).

Member 2 of the SPF at the Trendall locality contains bedded and stromatolitic dolomite with molar Fe/(Mg+Fe) = 0 to 0.1 (Appendix 2 and Supplementary Table 7 in Cammack, 2015). These rocks are partially-silicified and can be seen to grade into adjacent fully-silicified counterparts (Van Kranendonk, 2011: Supplementary Figures 2 A-E). The fully silicified stromatolitic samples contain mm- to μm-scale rhombic cavities, some with dolomite rhombs and some with chalcedony pseudomorphs (Supplementary Figures 3 E, F).

Hydrothermal chert veins cut across the bedded SPF rocks and branch into smaller quartz veins that have silicified the adjacent carbonates to form what appear as “bedded” cherts (Figure 3 and Supplementary Figure 2). In thin-section and by backscattered electron imaging (BSE) on a scanning electron microscope (SEM), the bedded dolomites are coarse and re-crystallized into 200 - 700 μm crystals. Locally, ferroan dolomite zonation occurs at contacts with quartz veins (Appendix 2 in Cammack, 2015). Despite re-crystallization, dolomites have LREE depletion, elevated Y/Ho and positive La, Gd and Er anomalies relative to chondrites that suggest dolomite precursors precipitated from Archean seawater (Table 1, Figures 9b, c and 10 of Van

Kranendonk et al., 2003).

Van Kranendonk and Pirajno (2004) analyzed the geochemistry and field relations of the Euro Basalt above the Strelley Pool Formation and volcanic rocks immediately beneath the SPF. They noted that hydrothermal alteration of the overlying Euro Basalt was low to absent. However, lenses in the Warrawoona Group immediately beneath the SPF are depleted in CaO and Na_2O and have slight enrichments of K_2O and Al_2O_3, as well as HREE-depleted geochemical patterns. They interpreted these trends as argillic and phyllic alteration by hydrothermal fluids that may have been responsible for some of the silicification in the Strelley Pool Formation. Hydrothermal pyrophyllite and phyllic alteration has also been detected by short wave infrared spectroscopy directly beneath the SPF at the Trendall Locality (Brown et al. 2004, 2006).

Boorn et al. (2007, 2010) analyzed δ^{30}Si and trace elements in Pilbara Kitty's Gap Chert. Based on differing trends of δ^{30}Si versus Al_2O_3, they interpreted some cherts as volcanogenic sediments that have been silicified by hydrothermal activity, and others as seawater-precipitated with low volcanogenic input.

All of the cross-cutting veins observed in this study terminate within the SPF (Figure 3), indicating that hydrothermal alteration occurred prior to the deposition of the Euro Basalt and may have been synchronous with deposition of the SPF (see also Sugitani et al., 2015).

Metamorphism

Metamorphism and hydrothermal alteration in East Pilbara terrane greenstones is locally variable. Metamorphic grade is generally low (prehnite-pumpellyite to lower greenschist facies), but increases to lower amphibolite facies at contacts of granitoid bodies (hornblende-plagioclase, with local actinolite-garnet). Cummingtonite-grunerite amphiboles in cherts at Camel Creek

(Supplementary Figure 4) indicate contact metamorphism adjacent to the Corunna Downs granitic complex (Cammack, 2015). More generally, the Strelley Pool Formation is typically reported to have experienced lower- to sub-greenschist facies regional metamorphism (Van Kranendonk, 2000; Van Kranendonk and Hickman, 2000; Terabayashi et al., 2003; Van Kranendonk and Pirajno, 2004; Lindsay et al., 2005; Brasier et al., 2006; Wacey et al., 2010).

Microquartz and chalcedony are present in cherts at the Trendall locality. These cements would have re-crystallized to polygonal megaquartz or undulatory megaquartz if heated to greenschist facies regional metamorphism. Likewise, the presence of grains sutured by pressure-solution, syntaxial quartz-overgrowths, and microquartz sandstone cements found at Unconformity Ridge (Valley et al., 2015; Cammack, 2015) would likely have re-crystallized to coarse or polygonal quartz during greenschist-facies metamorphism (Summer and Ayalon, 1995; Holness and Watt, 2001).

Thermal maturity of Organic Matter in the SPF

Raman spectra for carbonaceous matter provides an index of temperature, but are influenced by other factors including time, deformation and fluids (e.g., Wopenka and Pasteris, 1993; Jehlička et al., 2003). Organic matter in the M1 basal sandstone of the SPF at Unconformity Ridge has Raman spectra interpreted to record lower greenschist facies metamorphism (Wacey et al., 2011b). Organic matter in cherts sampled near the Trendall locality were also interpreted to record lower greenschist facies, with temperatures below 350^{o}C (Sugitani et al., 2013). However, Allwood et al. (2006b) found that temperatures estimated from organic matter in dolomite varies within a vertical transect of the SPF. They proposed that the stromatolitic M2 unit experienced temperatures less than 200^{o}C at Trendall, in contrast to adjacent samples of more permeable M1 and M3 that experienced up to ~400^{o}C. The variable temperature estimates from Raman indicate that the SPF has not uniformly experienced greenschist facies metamorphism and was heated locally by fluid advection (see also Van Kranendonk, 2006 and Terabayashi et al., 2003). The distinction of hydrothermal alteration vs. regional metamorphism is important and suggests that the unusual degree of preservation at the Trendall locality resulted because it escaped intense alteration and was only minimally affected by regional metamorphism.

Weathering and Silcretes

At the Trendall locality, dolomitic stromatolites of the Strelley Pool Formation are found near the base of a high chert ridge, along the banks of the Shaw River, which exposed fresher rocks. Stromatolites on ridge-crests across the whole of the East Pilbara Terrane are more completely silicified than in low-lying dolomitic outcrops near riverbanks, suggesting that some silicification at the Trendall locality and elsewhere may be related to weathering (Van Kranendonk, 2000; Hickman, 2008). Cenozoic weathering in the Pilbara region has been documented across Western Australia (Hocking and Cockbain, 1990). Li et al. (2012) found that U enrichment in the Apex Basalt is positively correlated with Fe^{3+}/Fe and occurred in the last 200 Myr as a result of oxidative weathering and meteoric water infiltration. Likewise, $^{40}Ar/^{39}Ar$ geochronology shows that K-Mn oxides from the Pilbara formed episodically as a result of Paleocene weathering (Dammer et al., 1999). These Cenozoic events may have been responsible for at least some of the silicification of the SPF.

Methods

Samples

Samples were collected and drilled in the lab with a 3-mm diamond coring bit and analyzed for $\delta^{18}O$ by laser fluorination (LF). Six Trendall locality samples were selected for more detailed in-situ analysis of $\delta^{18}O$ by SIMS. Sample information is in Supplementary Table 1. Sample locations, photographs and sketches of the Trendall locality can be found in Figure 3 and Supplementary Figure 2.

Microscopy

Each sample was examined by optical and scanning electron microscopy (SEM). Three to seven areas of interest for SIMS analysis (measuring ~500 by 350 μm) were selected in each sample based on examination of the different quartz textures. Optical images in plain and cross-polarized light (XPL) were made of each analysis area and SEM images were taken in backscattered electron (BSE) and cathodoluminescence (CL) modes using a Hitachi S3400 SEM at the Department of Geoscience, UW-Madison (Appendix 6 in Cammack, 2015). Unknown minerals were identified using energy dispersive X-ray spectrometry (EDS) on the SEM. In-situ spot analyses for chemical composition (EPMA), isotope ratios (SIMS), and corresponding imagery of analysis areas (SEM and petrographic microscope) have been managed using Quantum Geographic Information System (QGIS Development Team, 2014) (Appendix 3 in Cammack, 2015).

Oxygen Isotope Analysis

All $\delta^{18}O$ values are reported in standard permil (‰) notation relative to the Vienna Standard Mean Ocean Water Standard (VSMOW) (Baertschi, 1976; Coplen, 1988):

$$\delta^{18}O(\text{sample}) (‰, \text{VSMOW}) = 1000 * ([^{18}O/^{16}O]_{\text{sample}} / [^{18}O/^{16}O]_{\text{VSMOW}} - 1)$$

Laser Fluorination & Gas-source Mass Spectrometry (LF)

Samples were analyzed by laser fluorination and gas-source mass spectrometry (LF) at the Stable Isotope Laboratory, Department of Geoscience, UW-Madison. Preliminary selection was based on hand-sample observations of textural differences using a stereoscopic microscope.

Samples for LF were treated as needed to remove or aid in the identification of impurities (identified by microscopy) for 5 to 60 minutes with 15 molar HNO_3 (sulfides), 28 molar HF (silicates) and/or 12 molar HCl (carbonates). The HF treatment of quartz was used when other silicates were identified; HF was not intended to fully dissolve non-quartz silicates but to partially react, making them easier to avoid during preparation of splits for LF. Partial dissolution has no effect on $\delta^{18}O$ of residual quartz grains (Kelly et al., 2007). Final quartz separates were >99% pure. Purified quartz splits weighing 1-2 mg were individually loaded along with aliquots of UWG-2 garnet standard into a 70-sample nickel plug for LF analysis.

Bulk quartz samples were converted to CO_2 using a laser-heating and fluorination with the rapid-heating, defocused-beam technique. CO_2 was analyzed by Finnigan/MAT 251 triple-collecting gas-source mass-spectrometer (Valley et al., 1995; Spicuzza et al., 1998). Samples by LF were standardized with UWG-2 garnet standard ($\delta^{18}O$ = 5.80‰, Valley et al., 1995). External precision based on multiple analyses of UWG-2 on each day of analysis average ±0.10‰ (2SD) for all LF measurements reported here (Supplementary Table 2).

Secondary Ion Mass Spectrometry (SIMS)

SIMS analyses were made using a CAMECA IMS-1280. Procedures have been reported previously (Kelly et al., 2007; Kita et al., 2009; Valley and Kita, 2009); a brief description follows. Samples were mounted within 5 mm of the center of 25-mm diameter round samples and polished to a low-relief surface (Kita et al., 2009). One to two grains of UWQ-1 quartz standard ($\delta^{18}O$ = 12.33‰, Kelly et al., 2007) were cast near the center of each sample. An electron flood gun was used to aid charge neutralization at the C-coated sample surface. A $^{133}Cs^+$ beam with a sample current of ~ 2 nA was accelerated at 10 KeV (impact energy = 20 KeV) and focused on the sample surface to a diameter of ~10 μm (~1 μm deep) for each pit. Secondary O^-

ions were accelerated at -10 kV into a double-focusing, large-radius mass spectrometer where $^{16}O^-$ and $^{18}O^-$ ions were collected by two Faraday Cup detectors. A third Faraday Cup measured $^{16}O^1H$, which was resolved from ^{17}O. The average ratio of $^{16}O^1H/^{16}O$ from each UWQ-1 bracket was subtracted from each sample measurement to obtain background-corrected $^{16}O^1H/^{16}O$ values (Wang et al., 2014), that are used to monitor contamination and the possible presence of hydrous silica. Pits were pre-sputtered with the Cs beam for ~10 s prior to an automated routine that centered the secondary ion beam in the field aperture. For each pit, counting and integration was conducted for 80 s (20 cycles of 4s /ea.).

For each SIMS session, sample analyses were standardized every 5 to 17 measurements by bracketing with 8 to 12 spots on the UWQ-1 quartz standard. Spot-to-spot external repeatability of UWQ-1 averaged 0.24‰ 2SD and was at or below 0.5‰, 2SD for all reported data. SIMS $\delta^{18}O$ data are reported in Supplementary Table 3. After analysis, pits were imaged by SEM and petrographic microscope to verify the mineral texture that was analyzed and to exclude analyses that hit other phases or contaminants such as epoxy.

Results

Mineralogy

Most thin sections presented here are nearly 100% quartz. In some bedded M2 cherts from the Trendall locality, samples contained minor dolomite, siderite or late calcite veins and trace sulfides (Kozdon et al., 2010), apatite, barite, sericite, and Fe-Mn oxides. Partly silicified stromatolitic dolomites were also examined from Trendall that are composed of 0 to 50% quartz and 50 to > 90% dolomite (Cammack, 2015).

Quartz Textures and Petrology

Several textures of quartz were identified using plain light (PL), cross-polarized light

(XPL), and cathodoluminescence (CL) by SEM. Representative photomicrographs of quartz textures are shown in Figure 4 with corresponding XPL and CL images, showing SIMS analysis spots and values of $\delta^{18}O(Qz)$. Appendix 6 in Cammack (2015) has BSE, CL and XPL imagery of every SIMS analysis area and corresponding $\delta^{18}O(Qz)$ values.

Trendall Locality Textures

The textural definitions of microquartz, mesoquartz, and megaquartz described below are based on Folk and Weaver (1952) and Maliva et al. (2005). The textures and their relative timing at the Trendall locality were determined by optical and SEM petrography, and are listed in Table 1 and depicted in Figure 4.

Microquartz is commonly less than 10 µm in diameter. Mesoquartz has crystals from 20 to 50 µm. Microquartz and mesoquartz both have crenulated crystal boundaries and diffuse extinction in XPL. They are often associated with rhombohedral cavities, rhombohedral chalcedony pseudomorphs and occasional 2-200 µm dolomite crystals that are surrounded by either microquartz or mesoquartz (Supplementary Figure 3). Microquartz and mesoquartz typically exhibit dark or mottled CL textures (Figure 4A and B).

Megaquartz from the Trendall locality is greater than 50 µm in diameter with planar crystalline boundaries and sharp, non-undulose extinction in XPL. Megaquartz is divided into two categories: vein megaquartz and cavity megaquartz. It was not always possible to distinguish cavity vs. vein megaquartz in a 2D thin section. Megaquartz which was not distinguishable as vein megaquartz or cavity megaquartz was categorized as 'megaquartz' without a modifier (Figure 4C).

Vein megaquartz in 100 to 1000-µm wide veins is observed to cut all other textural varieties with the exception of cavity megaquartz at the Trendall locality (Supplementary Figure

5). It often surrounds 1-20 µm dolomite crystals (Supplementary Figure 3D) (identified using EDS) and occasionally contains ~1-3-µm, aqueous, fluid-vapor inclusions. It tends to be dark and massive or mottled in CL (Supplementary Figure 5).

Cavity megaquartz was only observed at the Trendall locality in M2. It is often drusy with euhedral crystal terminations that surround and point into the center of 50-250 µm rock cavities (Figure 5A). These rock cavities are occasionally rhombohedral (Supplementary Figures 3B and E). Oscillatory growth zoning is commonly seen in CL images of cavity megaquartz (Figure 5B). Some mesoquartz, commonly found near the basal sections of drusy cavity megaquartz, is distinctly bright and sometimes zoned when imaged with CL (Figure 4B).

Chalcedony from the Trendall locality occurs as radiating, fibrous, cavity filling cements and sandstone cements in M2 It is also found with vein megaquartz occurring near the contacts of the vein with the surrounding matrix. Occasionally it occurs as rhombohedral shapes (Supplementary Figure 3F). Chalcedony occurs throughout the SPF samples of this study as both length fast and length slow varieties. Chalcedony often exhibits dark, fibrous or mottled CL textures similar to microquartz (Figure 4C).

Laser Fluorination Oxygen Isotope Analyses (mm-scale)

Laser Fluorination (LF) measurements at mm-scale were conducted to regionally survey the $\delta^{18}O(Qz)$ of SPF cherts (Figure 6, Supplementary Table 2). Camel Creek has $\delta^{18}O(Qz)$ values that average 15.7‰, and show a relatively small range from 14.2 to 18.2‰ for 17 samples collected up to 400 m apart (Supplementary Table 2). Unconformity Ridge samples have an average $\delta^{18}O(Qz)_{LF}$ = 13.6 and range from 9.3 to 18.9‰. The Trendall locality (SPF) has significantly higher $\delta^{18}O(Qz)_{LF}$ values ranging from 13.7 to 25.7‰. Decimeter- to meter-scale hydrothermal veins at Trendall that cut chert bedding have average $\delta^{18}O(Qz)_{LF}$ = 15.6, and range from 14.9 to 16.1‰.

SIMS Oxygen Isotope Analyses (µm-scale)

Based on laser fluorination analyses, nine samples were selected for in-situ SIMS analysis (Figure 7). Six samples were from the Trendall locality, one from Camel Creek and two from Unconformity Ridge (Supplementary Table 1). Texturally homogenous foliated polygonal quartz (50-200 µm) in one sample from Camel Creek has low variability $\delta^{18}O$(Qz) (average = 15.5 ± 0.3‰, 2SD, N= 17). Analysis of two samples from outcrop on Unconformity Ridge, from near the stratigraphic top and bottom of M1, show that sandstone cements are also homogenous in $\delta^{18}O$ (ave. = 13.9 ± 0.4‰ 2SD, N=50). Detrital quartz $\delta^{18}O$ values are 10.0 to 13.8‰ and average 12.6‰ at Unconformity Ridge (Fig. 7A). The Trendall locality samples show an even greater, 24‰ range in $\delta^{18}O$(Qz) (7.3 to 31.3‰, N=252).

The SIMS $\delta^{18}O$ values of the different quartz textures are plotted as histograms for each sample location in Figure 7. Megaquartz and mesoquartz from Trendall have bimodal $\delta^{18}O$ distributions, and the histogram peaks correlate to high-$\delta^{18}O$, zoned, bright-CL vs. massive or mottled, dark-CL textures. Microquartz, chalcedony and vein megaquartz each exhibit unimodal distributions and have smaller ranges of $\delta^{18}O$ values. None of the chalcedony or quartz showed evidence for significant water in the background corrected OH measurements (Supplementary Figure 6). Tabulated SIMS data is in Supplementary Table 3.

Discussion

The Trendall locality yielded the most variable $\delta^{18}O$(Qz) of the areas sampled and is the focus of this section. Cammack (2015) reports detailed discussion and interpretation of the Unconformity Ridge and Camel Creek localities.

Textural and Temporal Oxygen Isotope Trends at the Trendall Locality

This section discusses the interpreted petrogenetic history of quartz textures at the Trendall locality, coupled with $\delta^{18}O$ analysis at µm-scale according to quartz textural type (Figure 7, Table 1).

Microquartz and Mesoquartz (earliest generation)

Low $\delta^{18}O$ mesoquartz and microquartz not only have similar values of $\delta^{18}O$ but exhibit a grain-diameter continuum without a discrete size-boundary. This suggests that mesoquartz has coarsened from earlier microquartz. Coarsening may have occurred heterogeneously within each sample resulting in microquartz and low $\delta^{18}O$ mesoquartz formation during a single hydrothermal event. Early formation of microquartz and most mesoquartz in the M2 bedded cherts at the Trendall locality is indicated, as these are cut by all other quartz textures (Table 1, Supplementary Figure 5). Microquartz is also indicated to be an early texture by the fine crystal sizes (<10 µm). Microquartz has an average $\delta^{18}O$ of 18.1‰, ranging from 15.6 to 21.9‰, which is similar to vein megaquartz (ave. $\delta^{18}O$ = 18.2‰; range = 14.4 - 21.2‰) (Figure 7D and G). Thus, it is possible that vein megaquartz formed after microquartz during early silicification.

Mesoquartz has a bimodal $\delta^{18}O$ distribution: low values are ~ 16 to 20‰ and high ~ 21 to 28‰ (Figure 7E). CL imaging distinguishes these textural types; there is a correlation of bright and zoned textures in the high $\delta^{18}O$ group, versus massive, mostly dark-CL textures in the low $\delta^{18}O$ mesoquartz (Figures 4B and 7E). On the basis of $\delta^{18}O$ and CL, these low- and high-$\delta^{18}O$ mesoquartz groups are interpreted to have formed in two events: early lower $\delta^{18}O$ hydrothermal alteration, typified by dark-mottled CL, and later high-$\delta^{18}O$ values were related to the formation of cavity megaquartz, typified by bright-zoned CL (as discussed below).

Megaquartz

High-$\delta^{18}O$, bright-zoned CL mesoquartz is often adjacent to the basal portions of cavity megaquartz crystals, which grows into voids (Figure 4B) and has similar $\delta^{18}O$ (Figure 7E and H). Due to this concentric association surrounding cavity megaquartz, the high $\delta^{18}O$ mesoquartz, which has similar bright and zoned CL textures, is interpreted to have exchanged $\delta^{18}O$ and coarsened through nucleation on what was previously microquartz from the same fluids as cavity megaquartz. Thus, high-$\delta^{18}O$ mesoquartz formed contemporaneously with cavity megaquartz and replaced microquartz (Table 1).

Cavity megaquartz and bright, CL-zoned mesoquartz were not observed to be cut by vein megaquartz (Supplementary Figure 5). Typical euhedral-drusy crystals surrounding and pointing into the center of 50-250 μm cavities (Figure 5) suggest cavity megaquartz formed after initial silicification of the SPF carbonates and is the youngest quartz texture at the Trendall locality (Table1). However, the absolute age of cavity megaquartz could not be established from textural observation. This generation of quartz could have formed from Precambrian hydrothermal fluids or, more recently, during weathering. The cavity megaquartz shows strong oscillatory zonation in CL (Figure 5B), similar to textures seen in quartz from hydrothermal ore deposits (Rusk et al., 2008) and in diagenetic cements in Paleozoic sandstone (Kelly et al., 2007; Pollington et al., 2016). Cavity megaquartz ranges in $\delta^{18}O$ from 17.9 to 31.3‰ and yields the highest average $\delta^{18}O$ (26.4‰) of any known chert in Archean-deposited sediments (Figures 1, 7H). The $\delta^{18}O(Qz)$ values in cavity megaquartz could form from $\delta^{18}O(water) \approx -5 \pm 5$‰. High $\delta^{18}O$ values are also reported for Eocene to Oligocene silcretes in the Lake Eyre Basin from east-central Australia (25-26‰, Alexandre et al., 2004) and for Paleozoic silcretes in Wisconsin (27-32‰, Kelly et al., 2007). Thus, the high $\delta^{18}O$ values and textural occurrence of cavity megaquartz at the Trendall locality are consistent with weathering, which was prevalent in Western Australia in the

Cenozoic (Hocking and Cockbain, 1990).

Vein megaquartz cuts all textural categories of quartz except cavity megaquartz and bright, CL-zoned mesoquartz. Therefore, veins form earlier than these textures and later, or penecontemporaneous with earlier quartz textures (e.g. microquartz and dark-CL mesoquartz) (Table 1, Supplementary Figure 5). Chalcedony (~ 5 µm thickness) is locally observed in thin section at the edges of quartz veins and thus formed contemporaneously with vein megaquartz. SIMS $\delta^{18}O$ analyses of vein megaquartz range from 14.4 to 21.2‰ (ave. = 18.2‰), similar to microquartz, chalcedony and low-$\delta^{18}O$ mesoquartz suggesting that megaquartz veins formed penecontemporaneously by the same fluids that replaced and silicified SPF carbonates in M2 (Figure 7D, E, G and I). Field evidence supports this conclusion; hydrothermal veins often interleave with overlying chert units at the Trendall locality and elsewhere in the SPF but do not crosscut the overlying Euro Basalt (Van Kranendonk and Pirajno, 2004; Hickman et al., 2011) (Figure 3 and Supplementary Figure 2).

Vein megaquartz in mm-scale veins from the Trendall locality has higher and more variable $\delta^{18}O$ (ave. = 18.2‰; range = 14.4 - 21.2‰ Figure 7G) than decimeter- to meter-scale veins (ave. $\delta^{18}O$ = 15.6‰; range = 14.9 - 16.1‰ Figure 6). The difference in $\delta^{18}O$ of small vs. large veins is expected if vein fluids cooled as they dispersed into smaller mm-scale conduits while permeating and exchanging with high-$\delta^{18}O$ sediments (Supplementary Figure 2). Thinner veins had lower fluid fluxes during exchange of low-$\delta^{18}O$ water with high-$\delta^{18}O$ dolomite (dolomite ave. = 18.4‰; Appendix 2 and Supplementary Tables 4 and 6 in Cammack, 2015). Thus, both lower temperatures and mixing would make thinner veins higher in $\delta^{18}O(Qz)$.

Chalcedony

Chalcedony at Trendall has low and unimodal values of $\delta^{18}O$ (ave. = 18.2 ±1.7‰ 2SD), strengthening the textural association with hydrothermal fluids that also formed vein megaquartz (Figure 7G and I). Chalcedony is often seen filling cavities and voids. It is observed as a first-stage cavity filling cement due to its occurrence at or near the edges of vein megaquartz. It may have formed by direct precipitation (Heaney, 1993) at the edges of hydrothermal conduits or by re-crystallization of a silica-gel precursor (Oehler, 1976) depending on temperature, crystallization rate, and degree of silica oversaturation (Williams and Crerar, 1985; Xu et al., 1998).

Detrital Quartz

Three outlier $\delta^{18}O(Qz)$ analyses from SPF member 2 (M2) cherts at the Trendall locality have $\delta^{18}O \approx 7.5‰$ (Figure 7A), similar to unaltered igneous quartz (King et al., 2000; Hoefs, 2015). The analyses are from rounded grains set in matrices of microquartz or mesoquartz (01MB35 - Area 2 and 5 from Cammack, 2015 – Appendix 6; CL images). Although detrital sand is rare in M2, it is common in M1 (not exposed at Trendall). For instance, the basal sandstone of the SPF (M1) that is well exposed on Unconformity Ridge is dominated by detrital quartz with zircons from ~ 3.51 Ga volcanic rocks in the underlying Coonterunah Subgroup (Valley et al., 2015).

Silicification of carbonate at the Trendall Locality: $\delta^{18}O(Qz)$

Quartz with petrographically early textures in M2 silicified dolomites (microquartz, low $\delta^{18}O$ mesoquartz, chalcedony; Table 1) has the lowest $\delta^{18}O$ values at the Trendall locality (~15-20‰, Figure 7D, E, I), similar to $\delta^{18}O$ reported in other studies of Archean chert. These values are more than 15‰ lower than quartz formed at equilibrium temperatures of 10-30°C if $\delta^{18}O(water) = -1‰$ ($\Delta^{18}O(Qz\text{-}H_2O) = 36.3\text{-}31.7‰$, Pollington et al. 2016, Supplementary Figure 1), and ~10‰ lower than $\delta^{18}O$ of Phanerozoic marine cherts (Figure 1). Both macroscopic

(Supplementary Figure 2) and microscopic textures at Trendall show that microquartz formed by silicification of carbonate. Detrital-carbonate grains in thin-section appear rarely in M2 (Allwood et al., 2006a), and are likely unrecognizable after silicification.

Bimodal $\delta^{18}O(Qz)$

As discussed earlier, the bimodal values of δ^{18}O(Qz) measured by SIMS (Figure 7J) show a strong correlation with textures imaged by SEM-CL. Quartz with bright CL and well-developed growth zoning (Figure 5B) has higher values of δ^{18}O from ~24 to 29‰, and quartz with dark CL and massive or mottled texture has lower values of δ^{18}O from ~15 to 20‰. These relations lead to a new understanding of the high δ^{18}O values at Trendall, first discovered by laser fluorination analysis of mm-scale samples and initially interpreted as Archean. The LF data show that values of δ^{18}O for quartz are higher and more variable at the Trendall locality than Camel Creek, Unconformity Ridge, or any other Archean cherts (Figures 1 and 6). LF data include values of δ^{18}O(Qz) up to 25.7‰, that are the highest LF data known for Mesoarchean chert (above the upper limit in Figure 1). SIMS μm-scale analyses show more variability and even higher values of up to 31.3‰. More importantly, the SIMS data reveal bimodality for the first time in Precambrian cherts. The majority of quartz with bright-CL and textures indicating late growth has the higher values of δ^{18}O above 24‰, whereas most of the dark-CL, early quartz has values below 20‰ (Figure 7).

Hydrothermal Activity vs. Metamorphism

Petrographic investigations coupled with SIMS analyses at Trendall reveal δ^{18}O(Qz) values at mm- to μm-scale that correlate to specific chert textures and preserve μm-scale δ^{18}O variability that would have been homogenized by metamorphism. In contrast, μm-scale δ^{18}O(Qz) analyses in cherts from one sample at Camel Creek (Cammack, 2015) are homogenous (15.5 ±

0.3‰ 2SD, N = 17) due to recrystallization during contact metamorphism from the Corunna Downs granite and homogenization of $\delta^{18}O$ at sub-meter-scale at this locality (Figure 7). Likewise, the LF data over a distance of 400m at Camel Creek are the least variable in this study (Figure 6). The cummingtonite-grunerite amphiboles at this locality (Supplementary Figure 4) suggest this rock could be a silicified mafic rock at high metamorphic grade. Clearly the Trendall locality experienced lower metamorphic grades than Camel Creek.

The Secular-temporal trend of Chert $\delta^{18}O$

The apparent secular-temporal trend of $\delta^{18}O$ in chert (Figure 1) has been debated for over 50 years. In contrast to earlier work, this study resolves multiple generations of chert and show that none of them were precipitated from seawater and thus none of the oxygen isotope compositions reflect Archean seawater conditions. Outcrop evidence shows that dolomite was the primary deposit (in M2) at the Trendall locality, and was replaced by generations of quartz. Paleoarchean silicification by penecontemporaneous hydrothermal activity is indicated by the presence of hydrothermal chert veins that cut up through, but do not pass above the SPF. Ironically, the highest $\delta^{18}O(Qz)$ (cavity megaquartz, Figure 7H), which would traditionally be considered the best candidate for precipitation from seawater, is the youngest generation, and likely did not even form during the Archean, and certainly did not precipitate in thermal and isotopic equilibrium with seawater. Thus, an alternative explanation for the temporal-secular chert $\delta^{18}O$ trend (Figure 1) is that it may reflect different formation processes in Archean cherts vs. Phanerozoic cherts.

Phanerozoic Cherts

Many Phanerozoic cherts form from biogenic opaline precursors (diatoms, sponge spicules and radiolaria; Maliva et al., 1989). For instance, the Miocene Monterey Formation, California formed by diagenesis of diatomaceous oozes that accumulated on the margins of North America (Behl, 1999). Recrystallization of opaline precursors occurred at low temperature (17 to 21°C; Matheney and Knauth, 1993; Behl and Garrison, 1994) and generally result in $\delta^{18}O$ values that are lower than would be in equilibrium with ocean water at seawater temperatures.

Archean Cherts

Archean cherts such as those in the Onverwacht Group, South Africa and the Strelley Pool Formation, which are included in the secular $\delta^{18}O$ trend (Figure 1), are interbedded with volcanic successions that drove complex hydrothermal systems (e.g., Van Kranendonk, 2006). Archean cherts formed in many environments, but the secular chert $\delta^{18}O$ trend in figure 1 is heavily weighted toward Archean cherts collected from greenstone belts.

Archean chert in greenstone belts, such as the Strelley Pool Formation and those from the Onverwacht Group, are usually associated with local and/or regional evidence for hydrothermal activity (de Wit et al., 1982; Paris et al., 1985; Westall et al., 2001; Brown et al., 2004; Van Kranendonk and Pirajno, 2004; Van Kranendonk, 2006; de Wit et al., 2011). At the Trendall locality, the Strelley Pool Formation is less intensely altered than in most other areas, but has: hydrothermal chert veins that cut across and feed into "bedded" cherts that represent silicified carbonates (Figure 3 and Supplementary Figure 2); early microquartz that is similar in $\delta^{18}O$ to quartz veins (Figure 7); and quartz that has pseudomorphed carbonates (Supplementary Figure 3). Thus, Trendall locality cherts, excluding the late cavity megaquartz, originated from Paleoarchean hydrothermal activity that was at low temperatures, but distinctly warmer than seawater.

As discussed earlier, comparisons of $\delta^{18}O$ data from cherts of different age (Figure 1) implicitly assume that they formed in similar conditions. This has evoked considerable debate for

5 decades. Archean cherts in the present study did not precipitate directly from seawater. Numerous studies, have documented Archean cherts that experienced similarly complex, metamorphic, diagenetic, and hydrothermal petrogenetic histories.

Conclusions

Detailed petrography and mm- to µm-scale measurements of $\delta^{18}O(Qz)$ lead to a new and more detailed understanding of petrogenesis for “bedded” cherts in the 3.4 Ga Strelley Pool Formation of the Pilbara Craton, Western Australia. Several generations of quartz are recognized and in-situ SIMS analyses reveal that $\delta^{18}O(Qz)$ values are variable at the µm-scale and correlate to petrographic textures. Bimodal $\delta^{18}O$ quartz analyses at the Trendall locality (Figure 7) reveal two events: 1) a Paleoarchean hydrothermal event which formed dark-mottled CL microquartz, mesoquartz, chalcedony and vein quartz with ($\delta^{18}O$ = ~15 to 20‰); 2) a relatively-recent, post-Archean, weathering event which formed bright, zoned CL cavity megaquartz and mesoquartz with values of uniquely high $\delta^{18}O$ for “Archean” host rocks ($\delta^{18}O$ = ~24 to 29‰). This richness of information was unknown in earlier studies that homogenized cm- to mm-scale samples for analysis of $\delta^{18}O$ by bulk methods.

Texture-specific, µm-scale $\delta^{18}O(Qz)$ values are strongly zoned and $\delta^{18}O(Qz)$ values differ at micrometer to kilometer scales in the Strelley Pool Formation. Paleoarchean sedimentary and authigenic features are unusually well preserved at the Trendall locality. Quartz at Trendall has the highest and most variable $\delta^{18}O$ values that have been reported in Archean cherts. At other localities hydrothermal alteration and contact metamorphism were driven by adjacent plutonic and volcanic rocks, and were variable in intensity. By contrast the Strelley Pool Formation at the Trendall locality preserves a low temperature oasis where hydrothermal activity was less intense than at other localities. These cherts preserve massive and stromatolitic dolomite, and relatively elevated $\delta^{18}O$ of early-formed textures (e.g., 15-20‰, microquartz, chalcedony); this differs from the SPF chert at Unconformity Ridge and Camel Creek (10-16‰).

The $\delta^{18}O$ values of earliest formed quartz within the Strelley Pool Formation does not record thermal or isotopic equilibrium with Archean seawater. The quartz in these cherts is seen at m- to μm-scale to replace earlier carbonates. We present a new hypothesis that the $\delta^{18}O$ record shown for chert in Figure 1 is biased due to the comparison of Archean cherts that may have formed by complex combinations of hydrothermal activity, metamorphism, and diagenetic cements, to younger cherts that mainly formed by diagenetic or biogenic processes in basinal settings. We challenge the traditional interpretations of this trend, and question whether samples in this trend are genuine seawater precipitates, products of hydrothermal activity, diagenetic cements, or a combination thereof. Detailed field observation and petrography coupled to in-situ isotope analysis by SIMS will allow this hypothesis to be tested in other cherts comprising the secular-temporal $\delta^{18}O$ trend.

Acknowledgments

We thank: Brian Hess for casting and polishing SIMS samples; David Valley for assistance in the 2001 Australia field-work; Julie Vry for petrography; Adam Denny and Ben Linzmeier who collaborated in developing QGIS techniques for plotting microanalytical data; Ben Linzmeier and Ryan Quinn who helped coding in 'R'; Maciej Śliwiński for developing ankerite SIMS standards; Andrée Valley who redrafted many of the figures; and John Fournelle and Phil Gopon who assisted with EPMA and SEM. Arthur Hickman publishes with permission of the Executive Director of the Geological Survey of Western Australia. This research was funded by the NASA Astrobiology Institute. WiscSIMS is funded by NSF (EAR-1355590) and UW-Madison. This is contribution number 1017 of the Australian Research Council Centre for

Excellence for Core to Crust Fluids, to which Martin Van Kranendonk is grateful for funding support.

References

Alexandre, A., Meunier, J.-D., Llorens, E., Hill, S.M., and Savin, S.M., 2004, Methodological improvements for investigating silcrete formation: petrography, FT-IR and oxygen isotope ratio of silcrete quartz cement, Lake Eyre Basin (Australia): Chemical Geology, v. 211, p. 261–274, doi: 10.1016/j.chemgeo.2004.06.024.

Allwood, A.C., Walter, M.R., Burch, I.W., and Kamber, B.S., 2007, 3.43 billion-year-old stromatolite reef from the Pilbara Craton of Western Australia: Ecosystem-scale insights to early life on Earth: Precambrian Research, v. 158, p. 198–227, doi: 10.1016/j.precamres.2007.04.013.

Allwood, A.C., Walter, M.R., Kamber, B.S., Marshall, C.P., and Burch, I.W., 2006a, Stromatolite reef from the Early Archaean era of Australia: Nature, v. 441, p. 714–718, doi: 10.1038/nature04764.

Allwood, A.C., Walter, M.R., and Marshall, C.P., 2006b, Raman spectroscopy reveals thermal palaeoenvironments of c. 3.5 billion-year-old organic matter: Vibrational Spectroscopy, v. 41, p. 190–197, doi: 10.1016/j.vibspec.2006.02.006.

Baertschi, P., 1976, Absolute ^{18}O content of standard mean ocean water: Earth and Planetary Science Letters, v. 31, p. 341–344, doi: 10.1016/0012-821X(76)90115-1.

Behl, R.J., 1999, Since Bramlette (1946): The Miocene Monterey Formation of California revisited: Classic Cordilleran Concepts: A View from California: Geological Society of America, Special Paper, v. 338, p. 301–313.

Behl, R.J., and Garrison, R.E., 1994, The origin of chert in the Monterey Formation of California (USA), *in* Siliceous, phosphatic and glauconitic sediments of the Tertiary and Mesozoic: Proceedings of the 29th International Geological Congress, Part C, p. 101–132.

Blake, R.E., Chang, S.J., and Lepland, A., 2010, Phosphate oxygen isotopic evidence for a temperate and biologically active Archaean ocean: Nature (London), v. 464, p. 1029–1032, doi: http://dx.doi.org.ezproxy.library.wisc.edu/10.1038/nature08952.

Bohrmann, G., Abelmann, A., Gersonde, R., Hubberten, H., and Kuhn, G., 1994, Pure siliceous ooze, a diagenetic environment for early chert formation: Geology, v. 22, p. 207–210, doi: 10.1130/0091-7613(1994)022<0207:PSOADE>2.3.CO;2.

Boorn, S.H.J.M. van den, van Bergen, M.J., Vroon, P.Z., de Vries, S.T., and Nijman, W., 2010, Silicon isotope and trace element constraints on the origin of ~3.5Ga cherts: Implications for Early Archaean marine environments: Geochimica et Cosmochimica Acta, v. 74, p. 1077–1103, doi: 10.1016/j.gca.2009.09.009.

Boorn, S.H.J.M. van den, Bergen, M.J. van, Nijman, W., and Vroon, P.Z., 2007, Dual role of seawater and hydrothermal fluids in Early Archean chert formation: Evidence from silicon isotopes: Geology, v. 35, p. 939–942, doi: 10.1130/G24096A.1.

Boyd, E.S., Hamilton, T.L., Spear, J.R., Lavin, M., and Peters, J.W., 2010, [FeFe]-hydrogenase in Yellowstone National Park: evidence for dispersal limitation and phylogenetic niche conservatism: The International Society for Microbial Ecology Journal, v. 4, p. 1485–1495, doi: 10.1038/ismej.2010.76.

Brasier, M.D., Antcliffe, J., Saunders, M., and Wacey, D., 2015, Changing the picture of Earth's earliest fossils (3.5–1.9 Ga) with new approaches and new discoveries: Proceedings of the National Academy of Sciences, v. 112, p. 4859–4864, doi: 10.1073/pnas.1405338111.

Brasier, M., Green, O., and Shields, G., 1997, Ediacaran sponge spicule clusters from southwestern Mongolia and the origins of the Cambrian fauna: Geology, v. 25, p. 303–306.

Brasier, M., McLoughlin, N., Green, O., and Wacey, D., 2006, A fresh look at the fossil evidence for early Archaean cellular life: Philosophical Transactions of the Royal Society of London B: Biological Sciences, v. 361, p. 887–902, doi: 10.1098/rstb.2006.1835.

Brock, T.D., and Brock, M.L., 1968, Measurement of Steady-State Growth Rates of a Thermophilic Alga Directly in Nature: Journal of Bacteriology, v. 95, p. 811–815.

Brown, AJ, Cudahy, TJ and Walter, MR, 2006, Hydrothermal Alteration at the Panorama Formation, North Pole Dome, Pilbara Craton, Western Australia: Precambrian Research, v. 151, p. 211-223.

Brown, A., Walter, M., and Cudahy, T., 2004, Short-Wave Infrared Reflectance Investigation of Sites of Paleobiological Interest: Applications for Mars Exploration: Astrobiology, v. 4, p. 359–376, doi: 10.1089/ast.2004.4.359.

Buick, R., and Dunlop, J.S.R., 1990, Evaporitic sediments of Early Archaean age from the Warrawoona Group, North Pole, Western Australia: Sedimentology, v. 37, p. 247–277, doi: 10.1111/j.1365-3091.1990.tb00958.x.

Buick, R., Dunlop, J.S.R., and Groves, D.I., 1981, Stromatolite recognition in ancient rocks: an appraisal of irregularly laminated structures in an Early Archaean chert-barite unit from North Pole, Western Australia: Alcheringa: An Australasian Journal of Palaeontology, v. 5, p. 161–181, doi: 10.1080/03115518108566999.

Buick, R., Groves, D.I., Dunlop, J.S.R., and Lowe, D.R., 1995, Abiological origin of described stromatolites older than 3.2 Ga: Comment and Reply: Geology, v. 23, p. 191–192, doi: 10.1130/0091-7613(1995)023<0191:AOODSO>2.3.CO;2.

Cammack, J.N., 2015, SIMS Microanalysis of the Strelley Pool Formation Cherts and the Implications for the Secular-Temporal Oxygen-isotope Trend of Cherts [MS thesis]: University of Wisconsin - Madison, 206 p.

Coplen, T.B., 1988, Normalization of oxygen and hydrogen isotope data: Chemical Geology: Isotope Geoscience section, v. 72, p. 293–297, doi: 10.1016/0168-9622(88)90042-5.

Cunningham, L.C., Page, F.Z., Simonson, B.M., Kozdon, R., and Valley, J.W., 2012, Ion microprobe analyses of $\delta^{18}O$ in early quartz cements from 1.9 Ga granular iron formations (GIFs); a pilot study: Precambrian Research, v. 214–215, p. 258–268, doi: http://dx.doi.org.ezproxy.library.wisc.edu/10.1016/j.precamres.2012.01.016.

Dammer, D., McDougall, I., and Chivas, A.R., 1999, Timing of weathering-induced alteration of manganese deposits in Western Australia; evidence from K/Ar and $^{40}Ar/^{39}Ar$ dating: Economic Geology, v. 94, p. 87–108, doi: 10.2113/gsecongeo.94.1.87.

Degens, E.T., and Epstein, S., 1964, Oxygen and carbon isotope ratios in coexisting calcites and dolomites from recent and ancient sediments: Geochimica et Cosmochimica Acta, v. 28, p. 23–44, doi: 10.1016/0016-7037(64)90053-5.

Degens, E.T., and Epstein, S., 1962, Relationship Between O^{18}/O^{16} Ratios in Coexisting Carbonates, Cherts, and Diatomites: American Association of Petroleum Geologists Bulletin, v. 46, p. 534–542.

Duda, J.-P., Kranendonk, M.J.V., Thiel, V., Ionescu, D., Strauss, H., Schäfer, N., and Reitner, J., 2016, A Rare Glimpse of Paleoarchean Life: Geobiology of an Exceptionally Preserved Microbial Mat Facies from the 3.4 Ga Strelley Pool Formation, Western Australia: PLOS ONE, v. 11, p. e0147629, doi: 10.1371/journal.pone.0147629.

Folk, R.L., and Weaver, C.E., 1952, A study of the texture and composition of chert: American Journal of Science, v. 250, p. 498–510, doi: 10.2475/ajs.250.7.498.

Gregory, R.T., 1991, Oxygen isotope history of seawater revisited; timescales for boundary event changes in the oxygen isotope composition of seawater (H. P. Taylor, J. R. O'Neil, & I. R. Kaplan, Eds.): Special Publication - Geochemical Society, v. 3, p. 65–76.

Gunnarsson, I., and Arnórsson, S., 2000, Amorphous silica solubility and the thermodynamic properties of $H_4SiO^\circ_4$ in the range of 0° to 350°C at P_{sat}: Geochimica et Cosmochimica Acta, v. 64, p. 2295–2307, doi: 10.1016/S0016-7037(99)00426-3.

Hamilton, T.L., Vogl, K., Bryant, D.A., Boyd, E.S., and Peters, J.W., 2012, Environmental constraints defining the distribution, composition, and evolution of chlorophototrophs in thermal features of Yellowstone National Park: Geobiology, v. 10, p. 236–249, doi: 10.1111/j.1472-4669.2011.00296.x.

Heaney, P.J., 1993, A proposed mechanism for the growth of chalcedony: Contributions to Mineralogy and Petrology, v. 115, p. 66–74, doi: 10.1007/BF00712979.

Hein, J.R., and Yeh, H.W., 1983, Oxygen-Isotope Composition of Secondary Silica Phases, Costa-Rica Rift Deep-Sea Drilling Project Leg-69: Initial Reports of the Deep Sea Drilling Project, v. 69, p. 423–429.

Hervig, R.L., 1992, Oxygen isotope analysis using extreme energy filtering: Chemical Geology: Isotope Geoscience section, v. 101, p. 185–186, doi: 10.1016/0009-2541(92)90216-R.

Hickman, A.H., 2008, Regional review of the 3426-3350 Ma Strelley Pool Formation, Pilbara Craton, Western Australia: Geological Survey of Western Australia, Record 2008/15, p. 27p.

Hickman, A.H., Van Kranendonk, M.J., Grey, K., 2011, State Geoheritage Reserve R50149 (Trendall Reserve), Geology and Evidence for Early Archean Life: GSWA Record 2011/10, 32 p.

Hocking, R.M., and Cockbain, A.E., 1990, Regolith, in Geology and Mineral Resources of Western Australia: Geological Survey of Western Australia, Memoir 3, p. 591–601.

Hoefs, J., 2015, Stable Isotope Geochemistry: Springer, 7th ed. 389 p. http://link.springer.com/chapter/10.1007/978-3-319-19716-6_2.

Hofmann, H.J., Grey, K., Hickman, A.H., and Thorpe, R.I., 1999, Origin of 3.45 Ga coniform stromatolites in Warrawoona Group, Western Australia: Geological Society of America Bulletin, v. 111, p. 1256–1262, doi: 10.1130/0016 7606(1999)111< 1256:OOGCSI >2.3. CO;2.

Holness, M.B., and Watt, G.R., 2001, Quartz recrystallization and fluid flow during contact metamorphism: a cathodoluminescence study: Geofluids, v. 1, p. 215–228, doi: 10.1046/j.1468-8123.2001.00015.x.

Jacob, D.E., 2004, Nature and origin of eclogite xenoliths from kimberlites: Lithos, v. 77, p. 295–316, doi: 10.1016/j.lithos.2004.03.038.

Jacob, D., Jagoutz, E., Lowry, D., Mattey, D., and Kudrjavtseva, G., 1994, Diamondiferous eclogites from Siberia: Remnants of Archean oceanic crust: Geochimica et Cosmochimica Acta, v. 58, p. 5191–5207, doi: 10.1016/0016-7037(94)90304-2.

Jaffrés, J.B.D., Shields, G.A., and Wallmann, K., 2007, The oxygen isotope evolution of seawater: A critical review of a long-standing controversy and an improved geological water cycle model for the past 3.4 billion years: Earth-Science Reviews, v. 83, p. 83–122, doi: 10.1016/j.earscirev.2007.04.002.

Jehlička, J., Urban, O., and Pokorný, J., 2003, Raman spectroscopy of carbon and solid bitumens in sedimentary and metamorphic rocks: Spectrochimica Acta Part A: Molecular and Biomolecular Spectroscopy, v. 59, p. 2341–2352, doi: 10.1016/S1386-1425(03)00077-5.

Karhu, J., and Epstein, S., 1986, The implication of the oxygen isotope records in coexisting cherts and phosphates: Geochimica et Cosmochimica Acta, v. 50, p. 1745–1756, doi: 10.1016/0016-7037(86)90136-5.

Kasting, J.F., 1993, Earth's early atmosphere: Science, v. 259, p. 920–926.

Kasting, J.F., Howard, M.T., Wallmann, K., Veizer, J., Shields, G., and Jaffrés, J., 2006, Paleoclimates, ocean depth, and the oxygen isotopic composition of seawater: Earth and Planetary Science Letters, v. 252, p. 82–93, doi: 10.1016/j.epsl.2006.09.029.

Kastner, M., Keene, J.B., and Gieskes, J.M., 1977, Diagenesis of siliceous oozes—I. Chemical controls on the rate of opal-A to opal-CT transformation—an experimental study: Geochimica et Cosmochimica Acta, v. 41, p. 1041–1059, doi: 10.1016/0016-7037(77)90099-0.

Keene, J.B., 1975, Cherts and porcellanites from the North Pacific, DSDP Leg 32: Initial Reports of the Deep Sea Drilling Project, v. 32, p. 429–507.

Kelly, J.L., Fu, B., Kita, N.T., and Valley, J.W., 2007, Optically continuous silcrete quartz cements of the St. Peter Sandstone: High precision oxygen isotope analysis by ion microprobe: Geochimica et Cosmochimica Acta, v. 71, p. 3812–3832, doi: 10.1016/j.gca.2007.05.014.

King, E.M., Valley, J.W., and Davis, D.W., 2000, Oxygen isotope evolution of volcanic rocks at the Sturgeon Lake volcanic complex, Ontario: Canadian Journal of Earth Sciences, v. 37, p. 39–50, doi: 10.1139/e99-106.

Kita, N.T., Ushikubo, T., Fu, B., and Valley, J.W., 2009, High precision SIMS oxygen isotope analysis and the effect of sample topography: Chemical Geology, v. 264, p. 43–57, doi: 10.1016/j.chemgeo.2009.02.012.

Knauth, L.P., 1992, Origin and diagenesis of cherts: An isotopic perspective, *in* Clauer, N. and Chaudhuri, S. eds., Isotopic Signatures and Sedimentary Records, Springer Berlin Heidelberg, Lecture Notes in Earth Sciences 43, p. 123–152, http://link.springer.com/chapter/10.1007/BFb0009863.

Knauth, L.P., 1994, Petrogenesis of chert: Reviews in Mineralogy, v. 29, p. 233–258.

Knauth, L.P., 2005, Temperature and salinity history of the Precambrian ocean: implications for the course of microbial evolution: Palaeogeography, Palaeoclimatology, Palaeoecology, v. 219, p. 53–69, doi: 10.1016/j.palaeo.2004.10.014.

Knauth, L.P., and Epstein, S., 1976, Hydrogen and oxygen isotope ratios in nodular and bedded cherts: Geochimica et Cosmochimica Acta, v. 40, p. 1095–1108, doi: 10.1016/0016-7037(76)90051-X.

Knauth, L.P., and Lowe, D.R., 2003, High Archean climatic temperature inferred from oxygen isotope geochemistry of cherts in the 3.5 Ga Swaziland Supergroup, South Africa: Geological Society of America Bulletin, v. 115, p. 566–580, doi: 10.1130/0016-7606(2003)115<0566:HACTIF>2.0.CO;2.

Kozdon, R., Kita, N.T., Huberty, J.M., Fournelle, J.H., Johnson, C.A., and Valley, J.W., 2010, In situ sulfur isotope analysis of sulfide minerals by SIMS: Precision and accuracy, with application to thermometry of ∼ 3.5 Ga Pilbara cherts: Chemical Geology, v. 275, p.

243–253, doi: 10.1016/j.chemgeo.2010.05.015.

Lepot, K., Williford, K.H., Ushikubo, T., Sugitani, K., Mimura, K., Spicuzza, M.J., and Valley, J.W., 2013, Texture-specific isotopic compositions in 3.4 Gyr old organic matter support selective preservation in cell-like structures: Geochimica et Cosmochimica Acta, v. 112, p. 66–86, doi: http://dx.doi.org.ezproxy.library.wisc.edu/10.1016/j.gca.2013.03.004.

Li, W., Johnson, C.M., and Beard, B.L., 2013, U–Th–Pb isotope data indicate Phanerozoic age for oxidation of the 3.4 Ga Apex Basalt: Earth and Planetary Science Letters, v. 319–320, p. 197–206, doi: 10.1016/j.epsl.2011.12.035.

Lindsay, J.F., Brasier, M.D., McLoughlin, N., Green, O.R., Fogel, M., Steele, A., and Mertzman, S.A., 2005, The problem of deep carbon—An Archean paradox: Precambrian Research, v. 143, p. 1–22, doi: 10.1016/j.precamres.2005.09.003.

Lowe, D.R., 1994, Abiological origin of described stromatolites older than 3.2 Ga: Geology, v. 22, p. 387–390, doi: 10.1130/0091-7613(1994)022<0387:AOODSO>2.3.CO;2.

Lowe, D.R., 1983, Restricted shallow-water sedimentation of early Archean stromatolitic and evaporitic strata of the Strelley Pool Chert, Pilbara Block, Western Australia: Precambrian Research, v. 19, p. 239–283.

Maliva, R.G., Knoll, A.H., and Siever, R., 1989, Secular change in chert distribution: a reflection of evolving biological participation in the silica cycle: Palaios, p. 519–532.

Maliva, R.G., Knoll, A.H., and Simonson, B.M., 2005, Secular change in the Precambrian silica cycle: Insights from chert petrology: Geological Society of America Bulletin, v. 117, p. 835–845, doi: 10.1130/B25555.1.

Marin, J., Chaussidon, M., and Robert, F., 2010, Microscale oxygen isotope variations in 1.9 Ga Gunflint cherts: Assessments of diagenesis effects and implications for oceanic paleotemperature reconstructions: Geochimica et Cosmochimica Acta, v. 74, p. 116–130, doi: 10.1016/j.gca.2009.09.016.

Marin-Carbonne, J., Robert, F., and Chaussidon, M., 2014, The silicon and oxygen isotope compositions of Precambrian cherts; a record of oceanic paleotemperatures? Precambrian Research, v. 247, p. 223–234, doi: http://dx.doi.org.ezproxy.library.wisc.edu/10.1016/j.precamres.2014.03.016.

Matheney, R.K., and Knauth, L.P., 1993, New isotopic temperature estimates for early silica diagenesis in bedded cherts: Geology, v. 21, p. 519–522, doi: 10.1130/0091-7613(1993)021<0519:NITEFE>2.3.CO;2.

Muehlenbachs, K., 1998, The oxygen isotopic composition of the oceans, sediments and the seafloor: Chemical Geology, v. 145, p. 263–273, doi: 10.1016/S0009-2541(97)00147-2.

Murata, K.J., and Nakata, J.K., 1974, Cristobalitic Stage in the Diagenesis of Diatomaceous Shale: Science, v. 184, p. 567–568.

Nelson, D.R., 1998, 142836: volcaniclastic sedimentary rock, Gorge Creek; Geochronology dataset 393393; in Compilation of geochronology data, June 2007 update: Geological Survey of Western Australia.

Nhleko, N., 2003, The Pongola Supergroup in Swaziland: Rand Afrikaans University, http://ujdigispace.uj.ac.za/handle/10210/1966.

Oehler, J.H., 1976, Hydrothermal crystallization of silica gel: Geological Society of America Bulletin, v. 87, p. 1143–1152, doi: 10.1130/0016-7606(1976)87<1143:HCOSG>2.0.CO;2.

Paris, I., Stanistreet, I.G., and Hughes, M.J., 1985, Cherts of the Barberton greenstone belt interpreted as products of submarine exhalative activity: The Journal of Geology, p. 111–129.

Perry Jr., E.C., and Lefticariu, L., 2007, Formation and Geochemistry of Precambrian Cherts, *in* Turekian, K.K. and Holland, H.D. eds., Treatise on Geochemistry, Oxford, Pergamon, p. 1–21, http://www.sciencedirect.com/science/article/pii/B0080437516071383.

Perry, E.C., and Tan, F.C., 1972, Significance of Oxygen and Carbon Isotope Variations in Early Precambrian Cherts and Carbonate Rocks of Southern Africa: Geological Society of America Bulletin, v. 83, p. 647–664, doi: 10.1130/0016-7606(1972)83[647:SOOACI]2.0.CO;2.

Pollington, A.D., Kozdon, R., Anovitz, L.M., Georg, R.B., Spicuzza, M.J., and Valley, J.W., 2016, Experimental calibration of silicon and oxygen isotope fractionations between quartz and water at 250 °C by in situ microanalysis of experimental products and application to zoned low δ^{30}Si quartz overgrowths: Chemical Geology, v. 421, p. 127–142, doi: 10.1016/j.chemgeo.2015.11.011.

Prokoph, A., Shields, G.A., and Veizer, J., 2008, Compilation and time-series analysis of a marine carbonate δ^{18}O, δ^{13}C, ^{87}Sr/^{86}Sr and δ^{34}S database through Earth history: Earth-Science Reviews, v. 87, p. 113–133, doi: 10.1016/j.earscirev.2007.12.003.

QGIS Development Team, 2014, QGIS Geographic Information System: Open Source Geospatial Foundation Project, http://qgis.osgeo.org/en/site/.

Riech, V., and von Rad, U., 1979, Silica Diagenesis in the Atlantic Ocean: Diagenetic Potential and Transformations, *in* Talwani, Manik, Hay, W., and Ryan, W.B.F. eds., Deep Drilling Results in the Atlantic Ocean: Continental Margins and Paleoenvironment, American Geophysical Union, p. 315–340, http://onlinelibrary.wiley.com.ezproxy.library.wisc.edu/doi/10.1029/ME003p0315/summary.

Robert, F., and Chaussidon, M., 2006, A palaeotemperature curve for the Precambrian oceans based on silicon isotopes in cherts: Nature, v. 443, p. 969–972, doi: 10.1038/nature05239.

Rouchon, V., and Orberger, B., 2008, Origin and mechanisms of K-Si-metasomatism of ca. 3.4-

3.3 Ga volcaniclastic deposits and implications for Archean seawater evolution: Examples from cherts of Kittys Gap (Pilbara craton, Australia) and Msauli (Barberton Greenstone Belt, South Africa): Precambrian Research, v. 165, p. 169-189, doi: 10.1016/j.precamres.2008.06.003.

Rusk, B.G., Lowers, H.A., and Reed, M.H., 2008, Trace elements in hydrothermal quartz: Relationships to cathodoluminescent textures and insights into vein formation: Geology, v. 36, p. 547–550, doi: 10.1130/G24580A.1.

Sagan, C., and Mullen, G., 1972, Earth and Mars: Evolution of Atmospheres and Surface Temperatures: Science, v. 177, p. 52–56, doi: 10.1126/science.177.4043.52.

Schwartzman, D.W., Knauth, P., Meech, K.J., Boss, A., and Irvine, W., 2007, A hot climate on early Earth; implications to biospheric evolution: Astrobiology, v. 7, p. 494, doi: http://dx.doi.org.ezproxy.library.wisc.edu/10.1089/ast.2007.1016.

Shields, G.A., 2007, Chapter 7.6 The Marine Carbonate and Chert Isotope Records and Their Implications for Tectonics, Life and Climate on the Early Earth, *in* Martin J. Van Kranendonk, R.H.S. and V.C.B. ed., Developments in Precambrian Geology, Elsevier, Earth's Oldest Rocks, v. 15, p. 971–983, http://www.sciencedirect.com/science/article/pii/S0166263507150763.

Shirey, S.B., and Richardson, S.H., 2011, Start of the Wilson cycle at 3 Ga shown by diamonds from subcontinental mantle: Science, v. 333, p. 434–436.

Siever, R., 1992, The silica cycle in the Precambrian: Geochimica et Cosmochimica Acta, v. 56, p. 3265–3272, doi: 10.1016/0016-7037(92)90303-Z.

Spicuzza, M.J., Valley, J.W., Kohn, M.J., Girard, J.P., and Fouillac, A.M., 1998, The rapid heating, defocused beam technique: a CO_2-laser-based method for highly precise and accurate determination of $\delta^{18}O$ values of quartz: Chemical Geology, v. 144, p. 195–203, doi: 10.1016/S0009-2541(97)00131-9.

Sugitani, K., Mimura, K., Nagaoka, T., Lepot, K., and Takeuchi, M., 2013, Microfossil assemblage from the 3400 Ma Strelley Pool Formation in the Pilbara Craton, Western Australia: Results form a new locality: Precambrian Research, v. 226, p. 59–74, doi: 10.1016/j.precamres.2012.11.005.

Sugitani, K., Mimura, K., Takeuchi, M., Yamaguchi, T., Suzuki, K., Senda, R., Asahara, Y., Wallis, S., and Van Kranendonk, M.J., 2015, A Paleoarchean coastal hydrothermal field inhabited by diverse microbial communities: the Strelley Pool Formation, Pilbara Craton, Western Australia: Geobiology, v. 13, p. 522–545.

Sugitani, K., Yamashita, F., Nagaoka, T., Yamamoto, K., Minami, M., Mimura, K., and Suzuki, K., 2006, Geochemistry and sedimentary petrology of Archean clastic sedimentary rocks at Mt. Goldsworthy, Pilbara Craton, Western Australia: Evidence for the early evolution of continental crust and hydrothermal alteration: Precambrian Research, v. 147, p. 124–147, doi: 10.1016/j.precamres.2006.02.006.

Summer, N.S., and Ayalon, A., 1995, Dike intrusion into unconsolidated sandstone and the development of quartzite contact zones: Journal of Structural Geology, v. 17, p. 997–1010, doi: 10.1016/0191-8141(95)00009-3.

Tartèse, R., Chaussidon, M., Gurenko, A., Delarue, F., and Robert, F., 2017, Warm Archaean oceans reconstructed from oxygen isotope composition of early-life remnants: Geochemical Perspectives Letters, p. 55–65, doi: 10.7185/geochemlet.1706.

Terabayashi, M., Masada, Y., Ozawa, H., 2003, Archean Ocean-floor Metamorphism in the North Pole area, Pilbara Craton, Western Australia: Precambrian Research, v. 127, p. 167-180, doi: 10.1016/S0301-9268(03)00186-4.

Valley, J.W., and Graham, C.M., 1996, Ion microprobe analysis of oxygen isotope ratios in quartz from Skye granite: healed micro-cracks, fluid flow, and hydrothermal exchange: Contributions to Mineralogy and Petrology, v. 124, p. 225–234, doi: 10.1007/s004100050188.

Valley, J.W., and Kita, N.T., 2009, In situ oxygen isotope geochemistry by ion microprobe: Mineralogical Association of Canada short course: secondary ion mass spectrometry in the earth sciences, v. 41, p. 19–63.

Valley, J.W., Kitchen, N., Kohn, M.J., Niendorf, C.R., and Spicuzza, M.J., 1995, UWG-2, a garnet standard for oxygen isotope ratios: Strategies for high precision and accuracy with laser heating: Geochimica et Cosmochimica Acta, v. 59, p. 5223–5231, doi: 10.1016/0016-7037(95)00386-X.

Valley, J.W., Lackey, J.S., Cavosie, A.J., Clechenko, C.C., Spicuzza, M.J., Basei, M.A.S., Bindeman, I.N., Ferreira, V.P., Sial, A.N., King, E.M., Peck, W.H., Sinha, A.K., and Wei, C.S., 2005, 4.4 billion years of crustal maturation: oxygen isotope ratios of magmatic zircon: Contributions to Mineralogy and Petrology, v. 150, p. 561–580, doi: 10.1007/s00410-005-0025-8.

Valley, J.W., Spicuzza, M.J., Cammack, J.N., Kitajima, K., Kita, N.T., and Van Kranendonk, M.J., 2015, Maturity of Archean Sandstones & Ancient Detrital Zircons: Goldschmidt Abstracts, p. 3220.

Van Kranendonk, M.J., 2000, Geology of the North Shaw 1: 100 000 sheet: Geological Survey of Western Australia, 1:100 000 Geological Series Explanatory Notes, 86 p.

Van Kranendonk, M.J., 2006, Volcanic degassing, hydrothermal circulation and the flourishing of early life on Earth: A review of the evidence from c. 3490-3240 Ma rocks of the Pilbara Supergroup, Pilbara Craton, Western Australia: Earth-Science Reviews, v. 74, p. 197–240, doi: 10.1016/j.earscirev.2005.09.005.

Van Kranendonk, M.J., 2011. Stromatolite morphology as an indicator of biogenicity for Earth's oldest fossils from the 3.5-3.4 Ga Pilbara Craton, Western Australia. In: Advances in Stromatolite Geobiology, edited by J. Reitner, N-V. Queric, and G. Arp. *Lecture Notes in Earth Sciences*, v. 131, Springer, Germany, pp. 517–534.

Van Kranendonk, M.J., and Hickman, A.H., 2000, Archaean geology of the North Shaw region, East Pilbara granite-greenstone terrane, Western Australia - a field guide: Geological Survey of Western Australia, Record 2000/5, p. 64.

Van Kranendonk, M.J., Hickman, A.H., Smithies, R.H., and Nelson, D.R., 2002, Geology and tectonic evolution of the Archean North Pilbara Terrain, Pilbara Craton, Western Australia (D. L. Houston, Ed.): Economic Geology and the Bulletin of the Society of Economic Geologists, v. 97, p. 695–732.

Van Kranendonk, M.J., and Pirajno, F., 2004, Geochemistry of metabasalts and hydrothermal alteration zones associated with c. 3.45 Ga chert and barite deposits: implications for the geological setting of the Warrawoona Group, Pilbara Craton, Australia: Geochemistry: Exploration, Environment, Analysis, v. 4, p. 253–278.

Van Kranendonk, M.J., Webb, G.E., and Kamber, B.S., 2003, Geological and trace element evidence for a marine sedimentary environment of deposition and biogenicity of 3.45 Ga stromatolitic carbonates in the Pilbara Craton, and support for a reducing Archaean ocean: Geobiology, v. 1, p. 91–108.

Veizer, J., Ala, D., Azmy, K., Bruckschen, P., Buhl, D., Bruhn, F., Carden, G.A.F., Diener, A., Ebneth, S., Godderis, Y., Jasper, T., Korte, C., Pawellek, F., Podlaha, O.G., et al., 1999, $^{87}Sr/^{86}Sr$, $\delta^{13}C$ and $\delta^{18}O$ evolution of Phanerozoic seawater: Chemical Geology, v. 161, p. 59–88, doi: 10.1016/S0009-2541(99)00081-9.

Veizer, J., and Hoefs, J., 1976, The nature of O^{18}/O^{16} and C^{13}/C^{12} secular trends in sedimentary carbonate rocks: Geochimica et Cosmochimica Acta, v. 40, p. 1387–1395, doi: 10.1016/0016-7037(76)90129-0.

Wacey, D., Kilburn, M.R., Saunders, M., Cliff, J., and Brasier, M.D., 2011a, Microfossils of sulphur-metabolizing cells in 3.4-billion-year-old rocks of Western Australia: Nature Geoscience, v. 4, p. 698–702, doi: 10.1038/ngeo1238.

Wacey, D., McLoughlin, N., Stoakes, C.A., Kilburn, M.R., Green, O.R., and Brasier, M.D., 2010, The 3426-3350 Ma Strelley Pool Formation in the East Strelley greenstone belt; a field and petrographic guide: Geological Survey of Western Australia, Record 2010/10, p. 64.

Wacey, D., Saunders, M., Brasier, M.D., and Kilburn, M.R., 2011b, Earliest microbially mediated pyrite oxidation in ~3.4 billion-year-old sediments: Earth and Planetary Science Letters, v. 301, p. 393–402, doi: 10.1016/j.epsl.2010.11.025.

Walker, J.C.G., and Lohmann, K.C., 1989, Why the oxygen isotopic composition of sea water changes with time: Geophysical Research Letters, v. 16, p. 323–326, doi: 10.1029/GL016i004p00323.

Wang, X.-L., Coble, M.A., Valley, J.W., Shu, X.-J., Kitajima, K., Spicuzza, M.J., and Sun, T., 2014, Influence of radiation damage on Late Jurassic zircon from southern China: evidence from in situ measurements of oxygen isotopes, laser Raman, U–Pb ages, and trace elements: Chemical Geology, v. 389, p. 122–136.

Wang, X., Hu, S., Gan, L., Wiens, M., and Müller, W.E.G., 2010, Sponges (Porifera) as living metazoan witnesses from the Neoproterozoic: biomineralization and the concept of their evolutionary success: Terra Nova, v. 22, p. 1–11, doi: 10.1111/j.1365-3121.2009.00909.x.

Wenzel, B., Lécuyer, C., and Joachimski, M.M., 2000, Comparing oxygen isotope records of Silurian calcite and phosphate—$\delta^{18}O$ compositions of brachiopods and conodonts: Geochimica et Cosmochimica Acta, v. 64, p. 1859–1872, doi: 10.1016/S0016-7037(00)00337-9.

Westall, F., de Wit, M.J., Dann, J., van der Gaast, S., de Ronde, C.E.J., and Gerneke, D., 2001, Early Archean fossil bacteria and biofilms in hydrothermally-influenced sediments from the Barberton greenstone belt, South Africa: Precambrian Research, v. 106, p. 93–116, doi: 10.1016/S0301-9268(00)00127-3.

Williams, L.A., and Crerar, D.A., 1985, Silica diagenesis; II, General mechanisms: Journal of Sedimentary Research, v. 55, p. 312–321, doi: 10.1306/212F86B1-2B24-11D7-8648000102C1865D.

Williams, G.E., and Schmidt, P.W., 1997, Paleomagnetism of the Paleoproterozoic Gowganda and Lorrain formations, Ontario: low paleolatitude for Huronian glaciation: Earth and Planetary Science Letters, v. 153, p. 157–169, doi: 10.1016/S0012-821X(97)00181-7.

de Wit, M.J., Furnes, H., and Robins, B., 2011, Geology and tectonostratigraphy of the Onverwacht Suite, Barberton Greenstone Belt, South Africa: Precambrian Research, v. 186, p. 1–27, doi: 10.1016/j.precamres.2010.12.007.

de Wit, M.J., Hart, R., Martin, A., and Abbott, P., 1982, Archean abiogenic and probable biogenic structures associated with mineralized hydrothermal vent systems and regional metasomatism, with implications for greenstone belt studies: Economic Geology, v. 77, p. 1783–1802.

Wopenka, B., and Pasteris, J.D., 1993, Structural characterization of kerogens to granulite-facies graphite: applicability of Raman microprobe spectroscopy: The American Mineralogist, v. 78, p. 533–557.

Xu, H., Buseck, P.R., and Luo, G., 1998, HRTEM investigation of microstructures in length-slow chalcedony: American Mineralogist, v. 83, p. 542–545.

Young, G.M., Brunn, V. von, Gold, D.J.C., and Minter, W.E.L., 1998, Earth's Oldest Reported Glaciation: Physical and Chemical Evidence from the Archean Mozaan Group (~2.9 Ga) of South Africa: The Journal of Geology, v. 106, p. 523–538, doi: 10.1086/516039.

Table 1: Quartz textures and relative timing for cementation in chert of the Strelley Pool Formation at the Trendall Locality.

Texture	Timing	Petrographic relations and Observations	Formation Hypotheses, Interpretations
Microquartz	1a	< 20 µm crystals, crenulated boundaries, diffuse extinction in XPL. Contains rhombohedral cavities surrounded by cavity megaquartz, local 1-200 µm dolomite. Cut by vein megaquartz, mesoquartz, and chalcedony. Dark-mottled CL.	First quartz generation. Replaces carbonate. Silicifying fluids supplied by decimeter-meter scale feeder veins infiltrating M2.
Mesoquartz (dark CL)	1b	> 20 µm crystals, crenulated boundaries. Often adjacent to microquartz. Contains rhombohedral-cavities, Local 1-200 µm dolomite. Cut by vein megaquartz. Dark-mottled CL.	Forms by hydrothermal fluid-microquartz interaction. This results in nucleation on and coarsening of microquartz during one or more silicification events with similar $\delta^{18}O$(fluid) and temperatures.
Chalcedony	1c	Forms at the edges of megaquartz veins. Also fills cavities. May form rhombohedral carbonate pseudomorphs in microquartz and mesoquartz. Length fast and slow varieties. Dark-mottled CL.	Similar $\delta^{18}O$(Qz) & petrographic relationships suggests a relationship with hydrothermal veins.
Megaquartz Veins	1d	> 50 µm crystals with planar boundaries and unit extinction. Crosscuts all other generations except cavity megaquartz. Occurs both as cm-m scale veins and mm-µm scale veins. Dark-mottled CL.	Fluid conduits replacing SPF carbonate protolith by hydrothermal fluids infiltrating and bifurcating into M2 bedded carbonates. $\delta^{18}O$ difference in outcrop scale vs. mm veins due to: cooling fluids, $\delta^{18}O$ fluid-carbonate exchange or different veining events.
Mesoquartz (bright CL)	2a	Associated with cavity megaquartz and often near the roots of the euhedral drusy crystals. Often bright in CL and zoned similar to cavity megaquartz. Not crosscut by veins.	Late nucleation & $\delta^{18}O$ exchange on microquartz. Related to cavity megaquartz formation event.
Cavity Megaquartz	2b	Found in <mm cavities. Euhedral drusy quartz crystal growths point into cavities. Not crosscut by veins. Bright and zoned in CL.	Late quartz cements likely related to weathering.

Abbreviations: XPL = crossed polarized light microscopy; CL = cathodoluminescence imaging; M1, M2 = SPF members 1, 2.

Figure Captions

Figure 1: Chert $\delta^{18}O$ secular-temporal trend through time. Data ranges from this study are shown at 3.4 Ga. Ages shown on this figure represent the depositional ages for the samples shown, and do not reflect the ages of alteration events affecting these cherts (see text). LF indicates bulk mm-sized laser-fluorination $\delta^{18}O$ analyses. The SIMS data represent measured cherts from the Trendall Locality that have elevated $\delta^{18}O$. Figure modified from Perry and Lefticariu (2007): $\delta^{18}O$ data and range for cherts (Knauth, 2005), chert $\delta^{18}O$ maximum (Robert and Chaussidon, 2006), carbonate $\delta^{18}O$ range (Shields and Veizer, 2002), zircon $\delta^{18}O$ upper limit (Valley et al., 2005).

Figure 2: Simplified geologic map of the East Pilbara Terrane of the Pilbara Craton, Western Australia, showing the Strelley Pool Formation sampling locations. A - Trendall Locality. B - Unconformity Ridge. C - Camel Creek. Base-map is from Hickman (2008).

Figure 3: A - Outcrop map of the Trendall Locality (from Van Kranendonk, 2011). The contact of bedded and stromatolitic M2 to overlying M3 detrital units is indicated. Red points labeled 'PA' to 'PF' correspond to outcrop photos in Supplementary Figure 2. Locations of parts 'B' and 'C' outlined in red boxes. B and C show detailed sampling locations (Sample numbers in white circles are preceded by 01MB in supplementary data tables; e.g. 41 = 01MB41) with their corresponding average laser fluorination $\delta^{18}O(Qz)$ values.

Figure 4: Strelley Pool Formation quartz textures with SIMS $\delta^{18}O$ analyses in matching XPL (Cross-polarized light optical microscopy) and CL (Cathodoluminescence) images. All scale bars = 50 µm. A to D are samples from the Trendall Locality. E is from Unconformity Ridge. A - microquartz and cavity megaquartz (sample 01MB41A). B -cavity megaquartz and mesoquartz (sample 01MB41B). C - chalcedony and megaquartz (sample 01MB42B). D - cavity megaquartz and vein megaquartz (sample 01MB42A). E - Sandstone, thin section is ~100 µm thick (sample 12-ABDP8@151.83). Abbreviations are: Chal = chalcedony, CM = cavity megaquartz, DQ = detrital quartz, MQ = microquartz, Mes = mesoquartz, Meg = megaquartz, VM = vein megaquartz. Bright white spots in CL images are from residual alumina polishing grit.

Figure 5: A – Scanning Electron Microscope image of cavity megaquartz from the Trendall locality (sample 01MB41). B - Cathodoluminescence image with zoned “cavity megaquartz” from the Trendall locality (sample 01MB33). The cavity has been colored black.

Figure 6: Boxplot comparing sampling locations $\delta^{18}O$ values at the mm-scale analyzed by laser fluorination. Boxes represent the 2nd and 3rd quartile range of $\delta^{18}O$ for each location. Dark vertical lines are the medians for the data. Whiskers represent the data range for each location. Individual $\delta^{18}O$ points are represented within the boxplot for each locality. See Supplementary Table 2 for tabulated data.

Figure 7: Histograms of SIMS $\delta^{18}O$ plotted by quartz textures defined by Cross-Polarized Light (XPL) and Cathodoluminescence (CL) analysis. Each histogram indicates a textural classification using either XPL (microquartz, mesoquartz, chalcedony, etc). Warm colors (oranges, red) indicate oscillatory zonation defined by CL, cool colors (blues) indicate mottled or

massive CL textures. See Supplementary Table 3 for tabulated data.

Supplementary Figure Text

Supplementary Figure 1: Values of $\delta^{18}O(Qtz)$ equilibrium from several $\delta^{18}O(H_2O)$ values at varying water temperature (Clayton et al. 1972; Friedman and O'Neil 1977).
Supplementary Figure 2: Silicification at the Trendall Locality. Photo locations are marked in Figure 2 by red points labeled 'PA' to 'PF'. A - Partial silicification of dolomite by cross-cutting hydrothermal vein that shows zonation from outer, black chert (microquartz) margin to inner, quartz core (see also Van Kranendonk and Barley, 2010). B and C – Stromatolitic, partially silicified dolomite (dark brown, raised parts) and non-silicified dolomite (light brown, recessive). D - Fully silicified stromatolites. E - Black hydrothermal vein cutting perpendicular to bedded, silicified (left of vein), and partially silicified (right of vein), stromatolitic dolomite (View looking east). F – Silicified sedimentary breccia/conglomerate in the M3 clastic unit.

Supplementary Figure 3: A - Dolomite rhombs with Fe-rich rims in quartz (sample 01MB35). B - Rhombohedral cavities (sample 01MB41). C - Dolomite rhomb in microquartz and mesoquartz (Sample 01MB35). D -Dolomite remnants in megaquartz (sample 01MB42). E – Irregular to rhombohedral cavities in microquartz (sample 01MB41). F - Chalcedony pseudomorphing carbonate (sample 01MB42). BSE = Back-scattered electron image; XPL = Cross polarized light microscopic view. Dol = Dolomite; Qtz = Quartz; FeDol = Iron-rich dolomite.

Supplementary Figure 4: Foliated metachert from Camel Creek samples. A - Lenticular aggregates of cummingtonite-grunerite in fine- to medium-grained, granoblastic quartz (sample 01MB22). B and C - Laths of cummingtonite-grunerite in quartz (sample 01MB15). D - Energy-dispersive X-ray spectroscopy (EDS) of cummingtonite-grunerite from point indicated on the BSE image in 'C'. BSE = Back-scattered electron image; XPL = Cross polarized light microscopic view. Qtz = Quartz; Cum-Gru = Cummingtonite-Grunerite amphiboles.

Supplementary Figure 5: Petrographic relationship between vein megaquartz (VM) and cavity megaquartz (CM) from sample 01MB41 at the Trendall Locality. The same cavity is highlighted in orange in all three images. Microquartz is labeled 'MQ'. SIMS $\delta^{18}O$ analyses are indicated by red points.

Supplementary Figure 6: A - SIMS plot of all quartz data. B - SIMS chalcedony data. Error bars indicate 2SD external precision. Values of $^{16}O^{1}H/^{16}O$ are background-corrected to the UWQ-1 quartz standard measurements for each bracket (average $^{16}O^{1}H/^{16}O$ of each bracket of standards was subtracted from the unknown $^{16}O^{1}H/^{16}O$ values in that bracket). See supplementary table 3 for tabulated data.

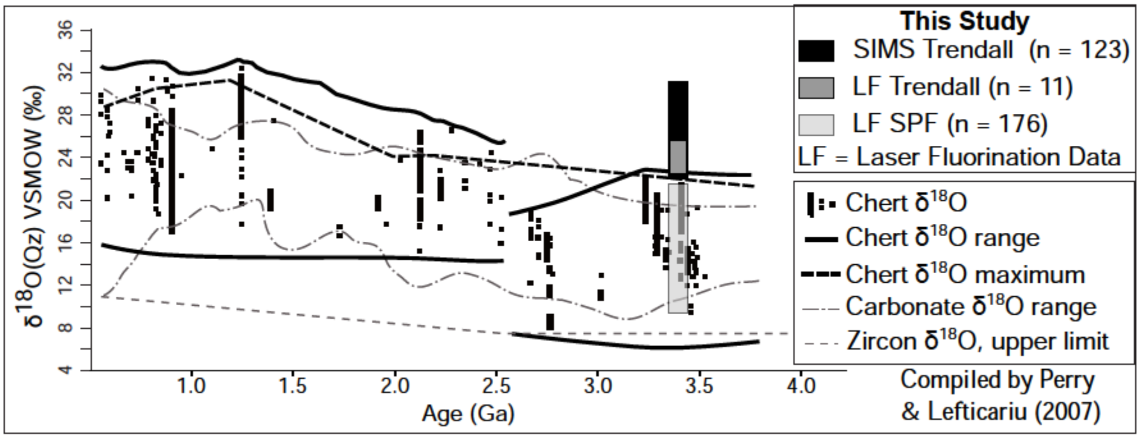

Figure 1: Figure text is in a separate document.

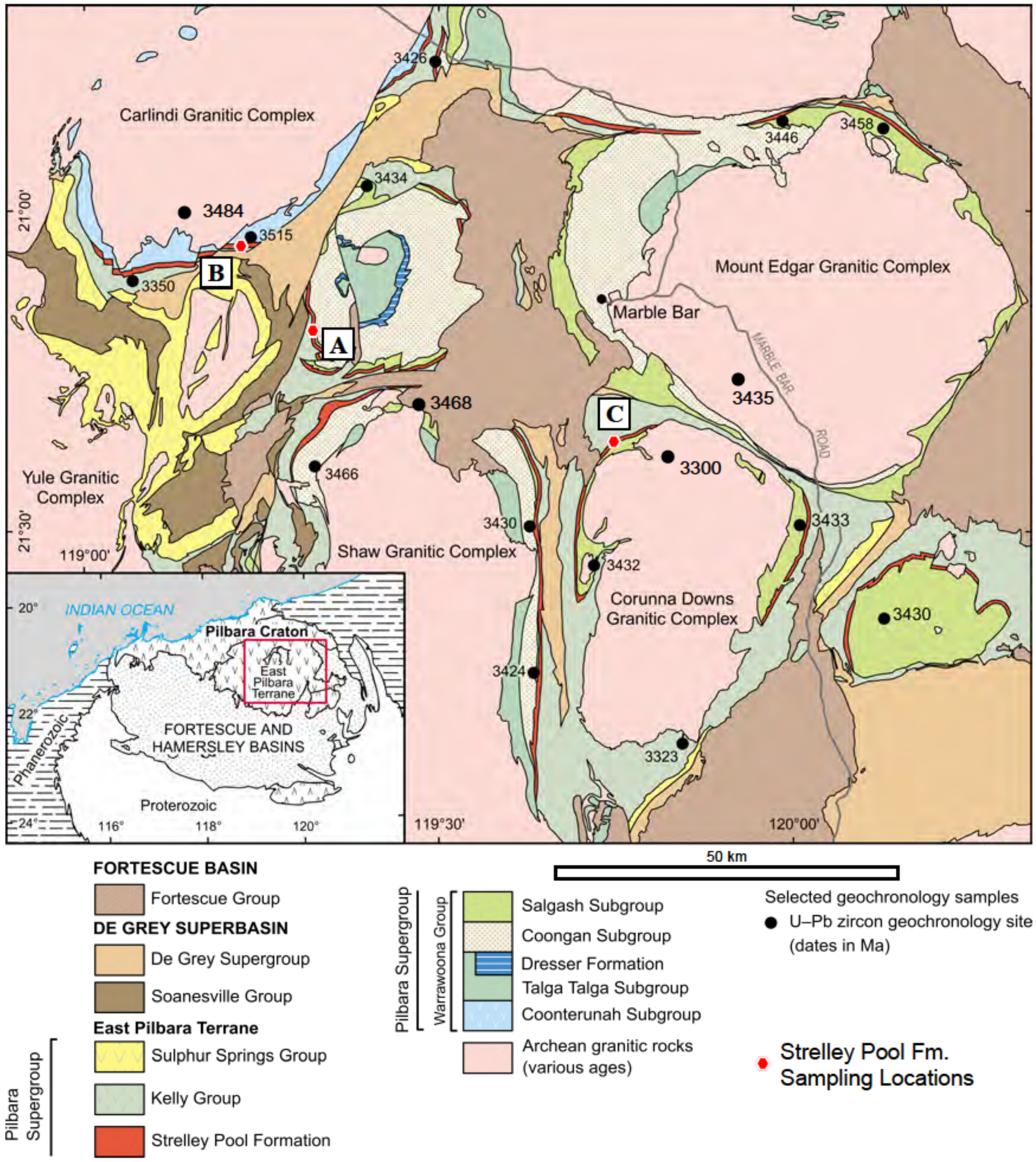

Figure 2: Figure text is in a separate document.

Figure 3:

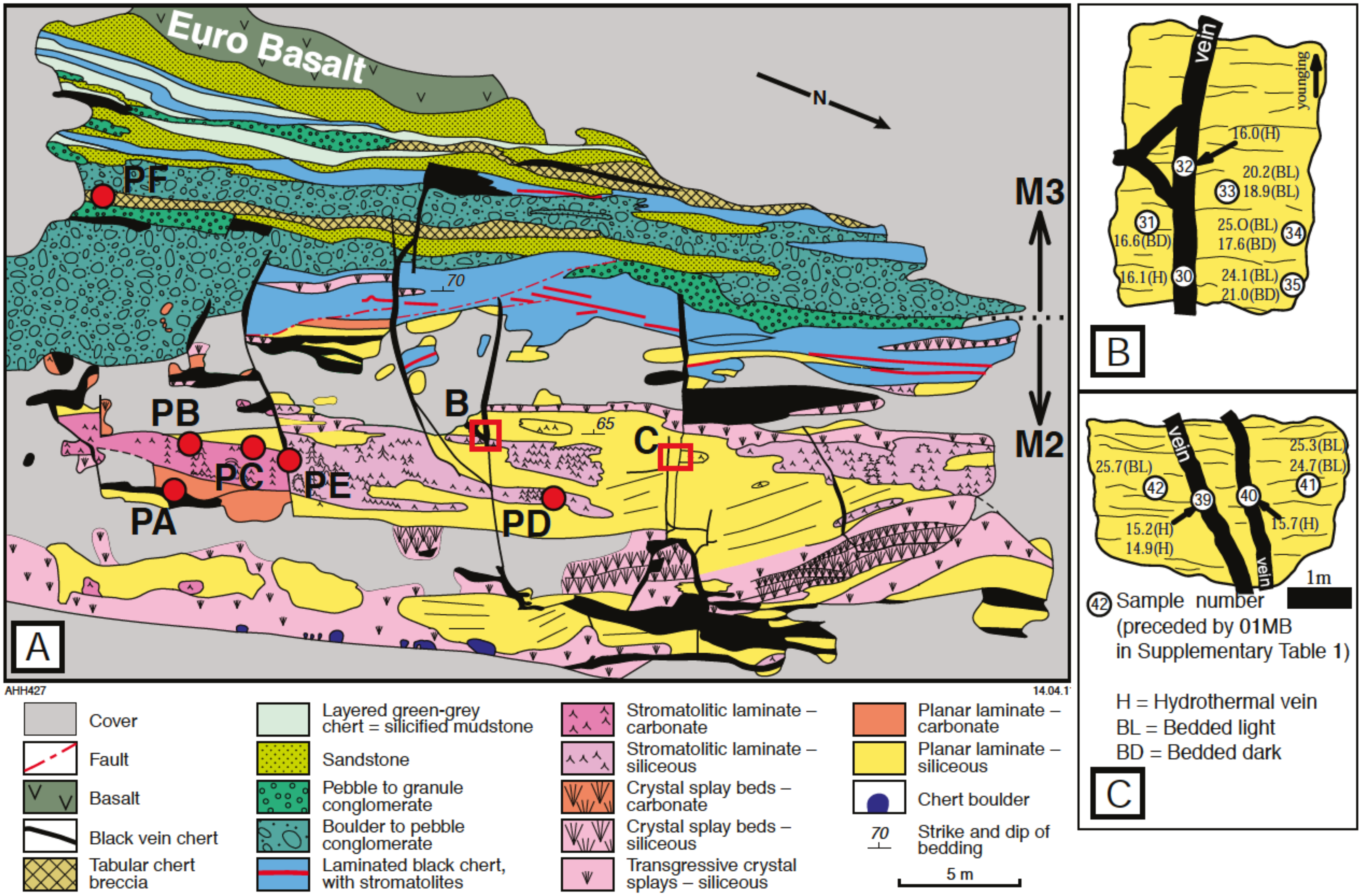

Euro Basalt
N
M3
M2
PF
PB
PC
PE
PA
PD
B
C
70
65
A
AHH427
14.04.1
Cover
Fault
Basalt
Black vein chert
Tabular chert breccia
Layered green-grey chert = silicified mudstone
Sandstone
Pebble to granule conglomerate
Boulder to pebble conglomerate
Laminated black chert, with stromatolites
Stromatolitic laminate – carbonate
Stromatolitic laminate – siliceous
Crystal splay beds – carbonate
Crystal splay beds – siliceous
Transgressive crystal splays – siliceous
Planar laminate – carbonate
Planar laminate – siliceous
Chert boulder
Strike and dip of bedding
5 m
vein
younging
16.0(H)
20.2(BL)
18.9(BL)
25.0(BL)
17.6(BD)
16.6(BD)
16.1(H)
24.1(BL)
21.0(BD)
32
33
31
34
30
35
B
vein
25.3(BL)
24.7(BL)
25.7(BL)
15.2(H)
14.9(H)
15.7(H)
42
39
40
41
1m
Sample number (preceded by 01MB in Supplementary Table 1)
H = Hydrothermal vein
BL = Bedded light
BD = Bedded dark
C

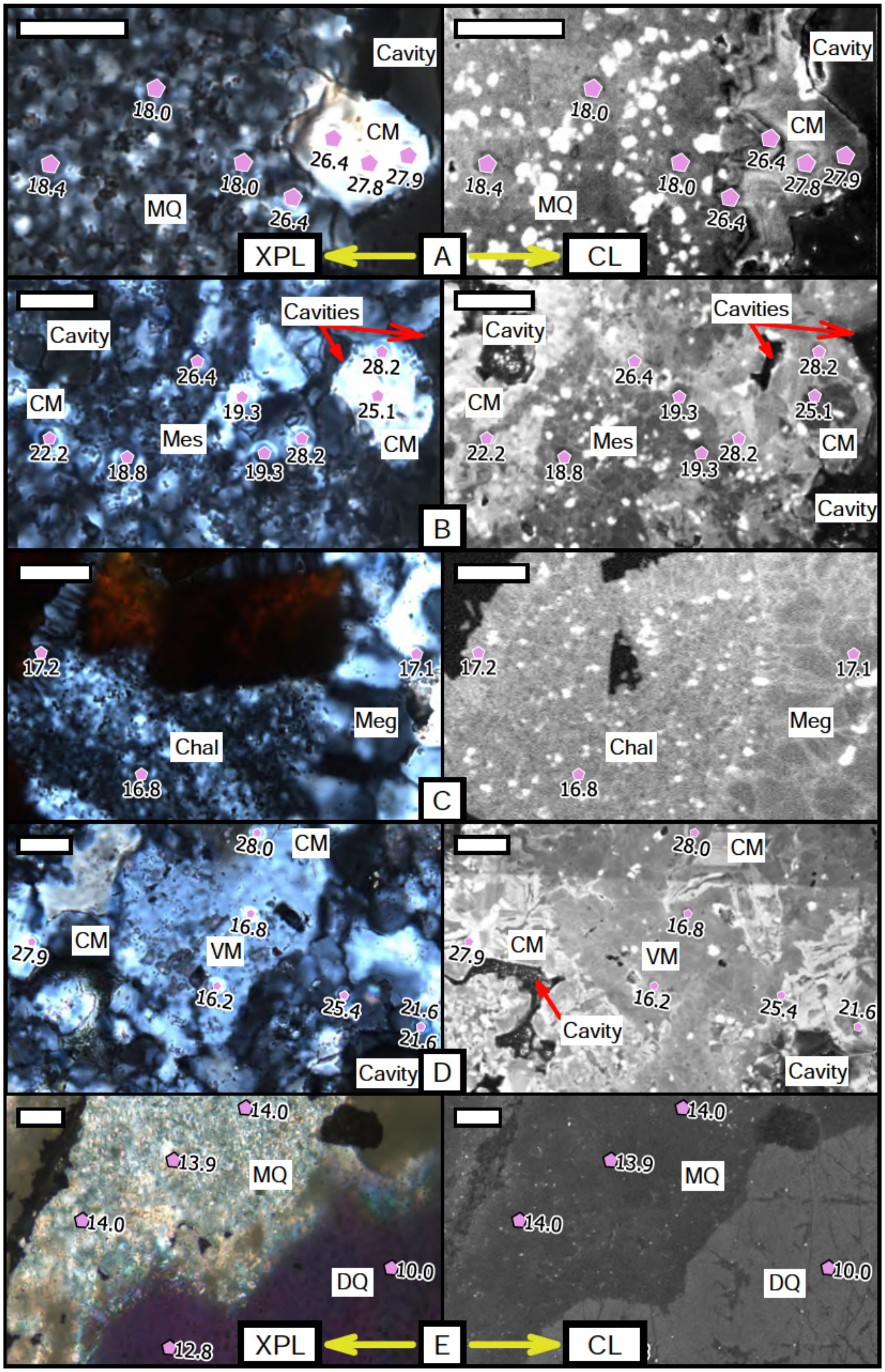

Figure 4: Figure text is in a separate document.

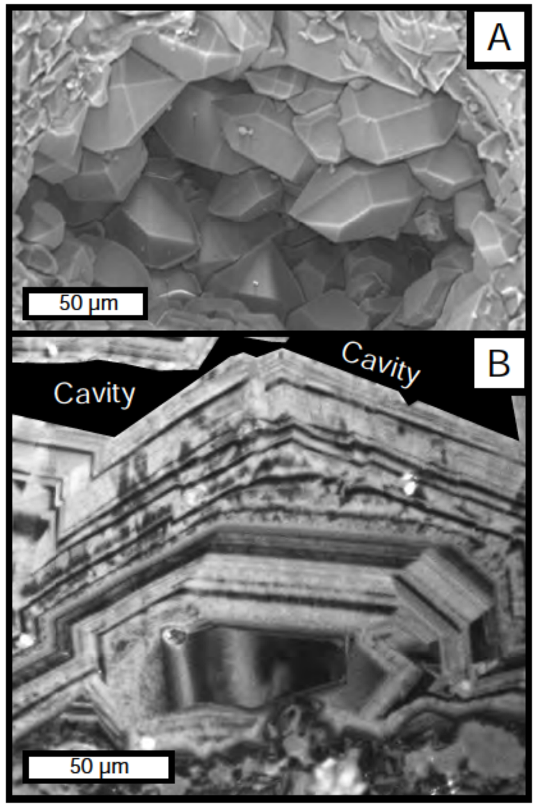

Figure 5: Figure text is in a separate document.

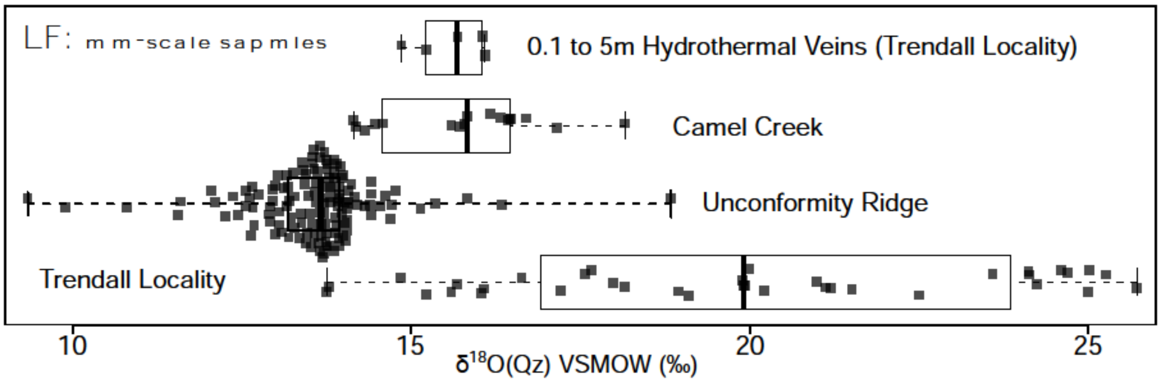

Figure 6: Figure text is in a separate document.

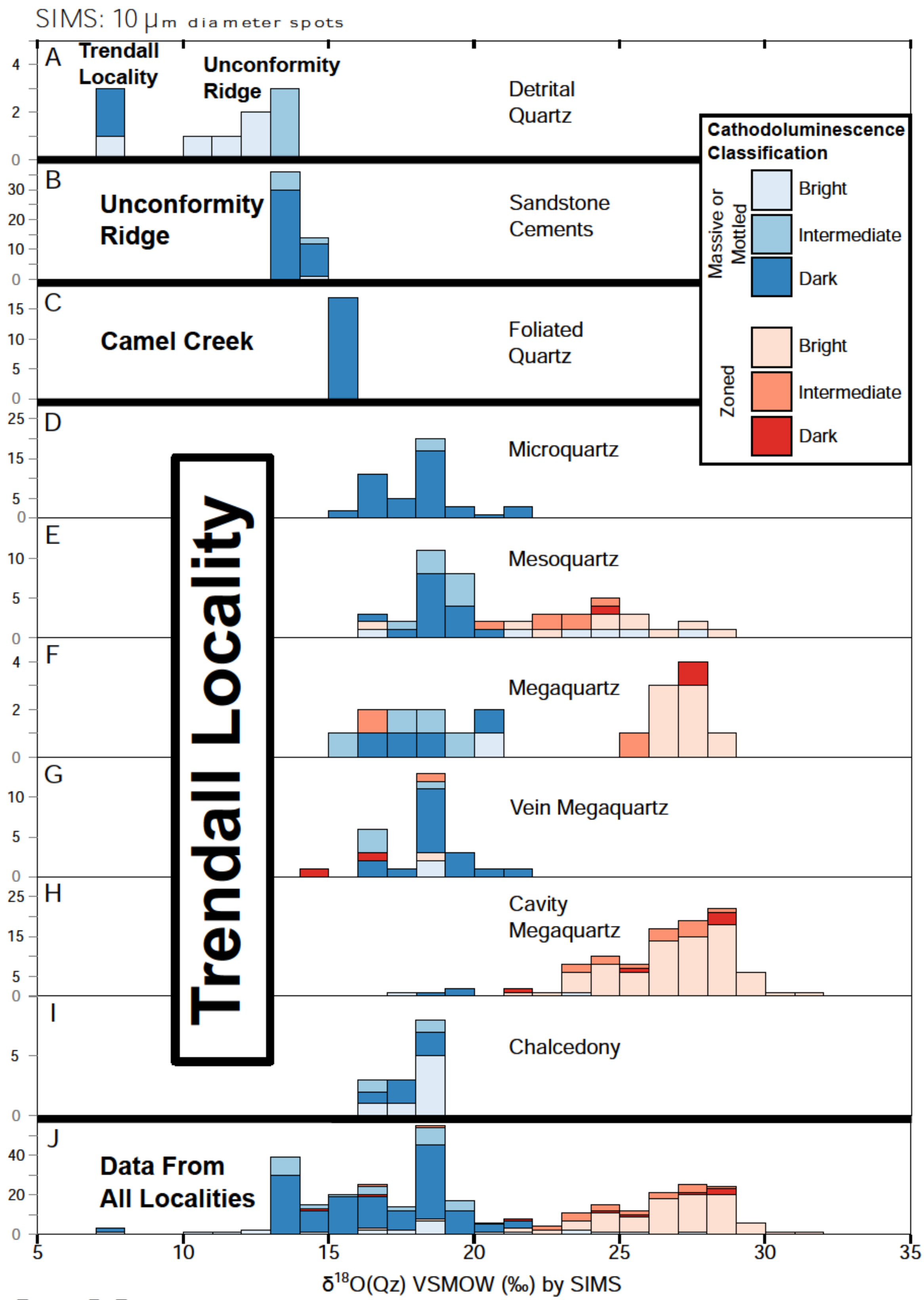

Figure 7: Figure text is in a separate document.

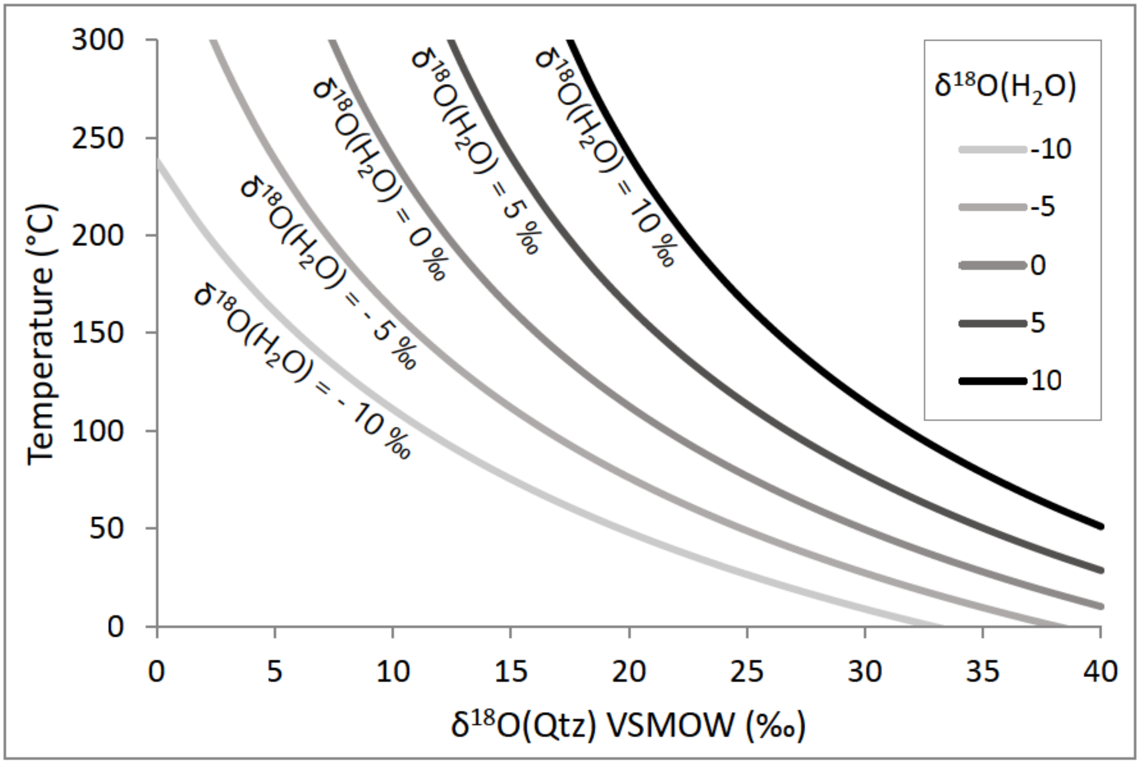

Supplementary Figure 1: Figure text is in a separate document.

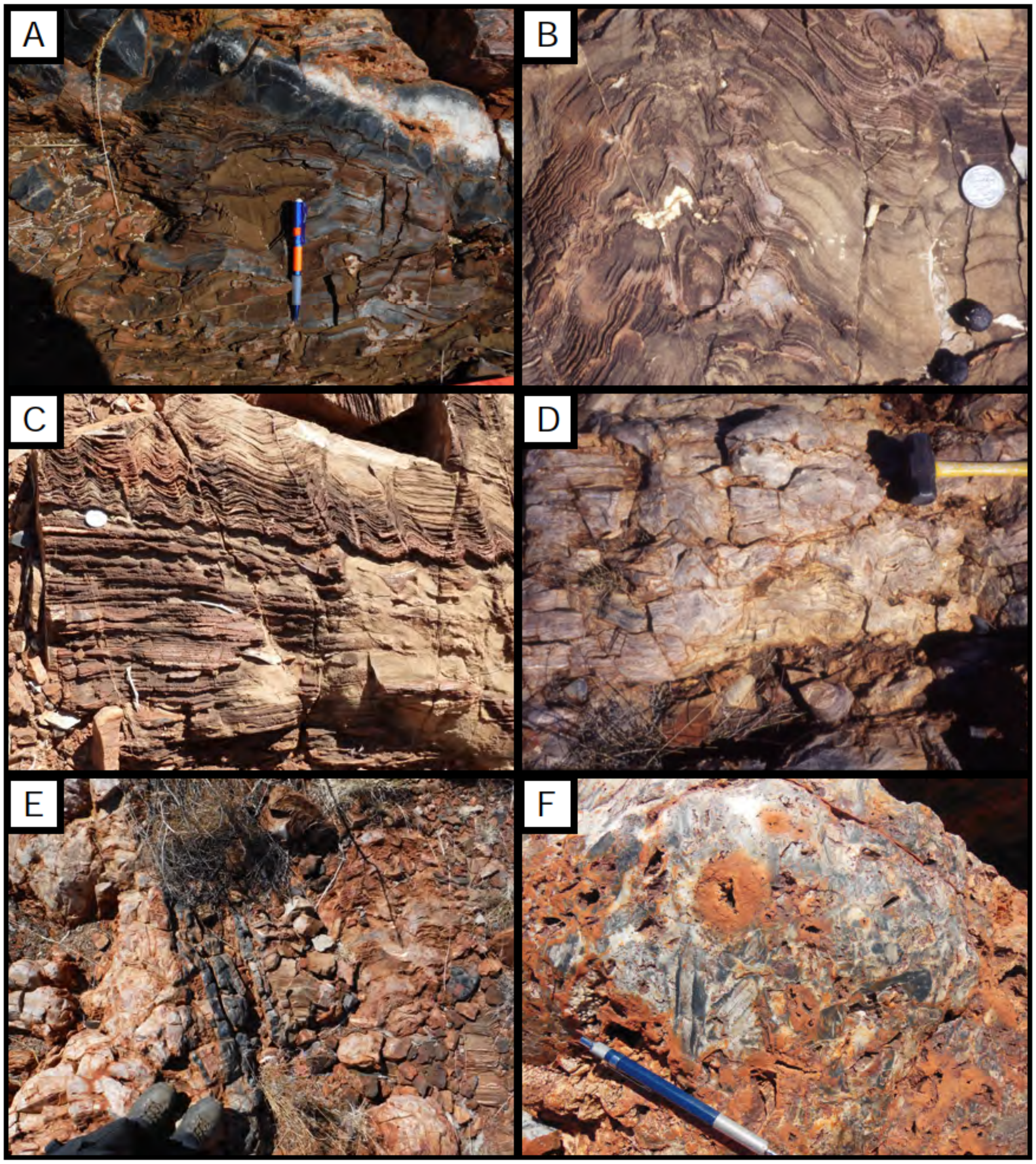

Supplementary Figure 2: Figure text is in a separate document.

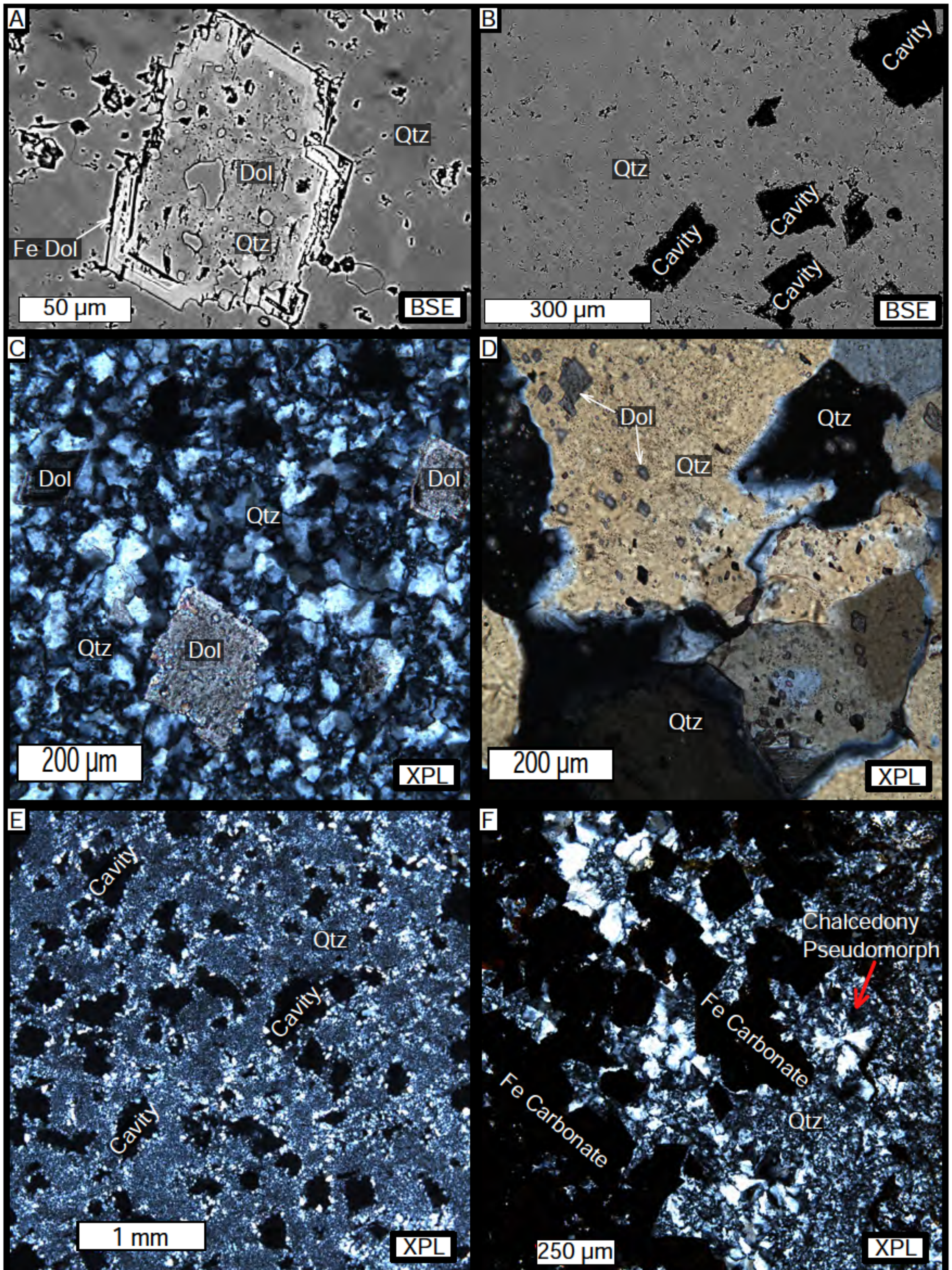

Supplementary Figure 3: Figure text is in a separate document.

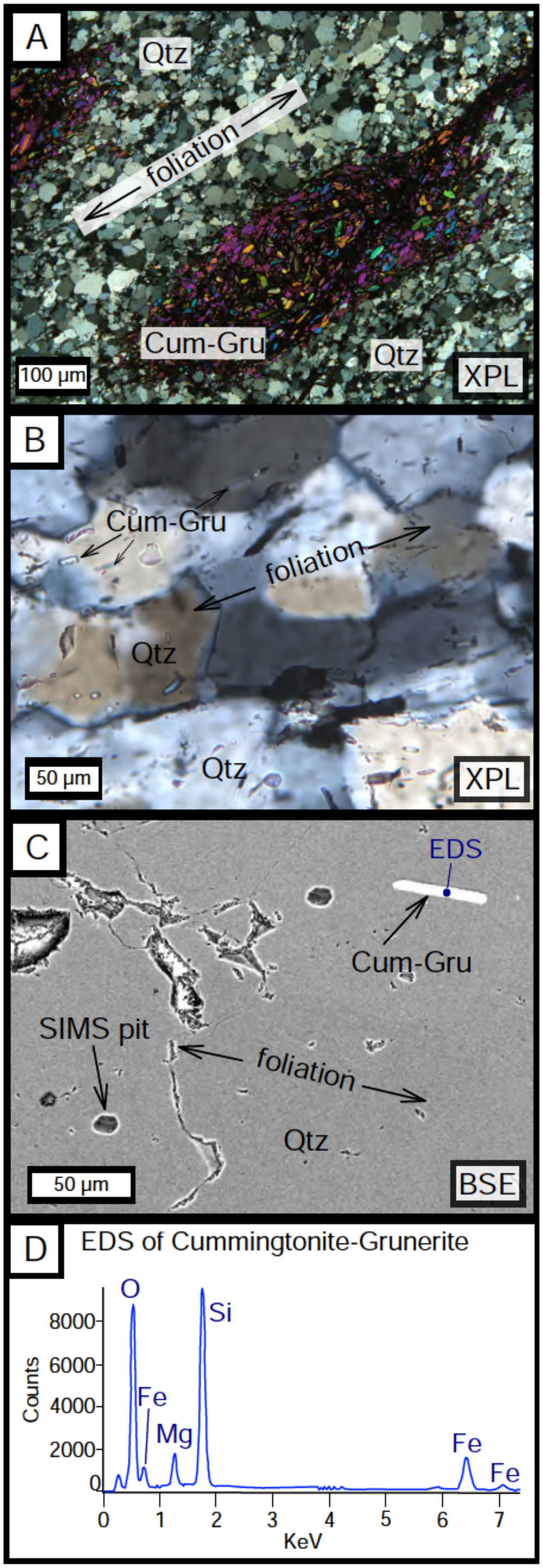

Supplementary Figure 4: Figure text is in a separate document.

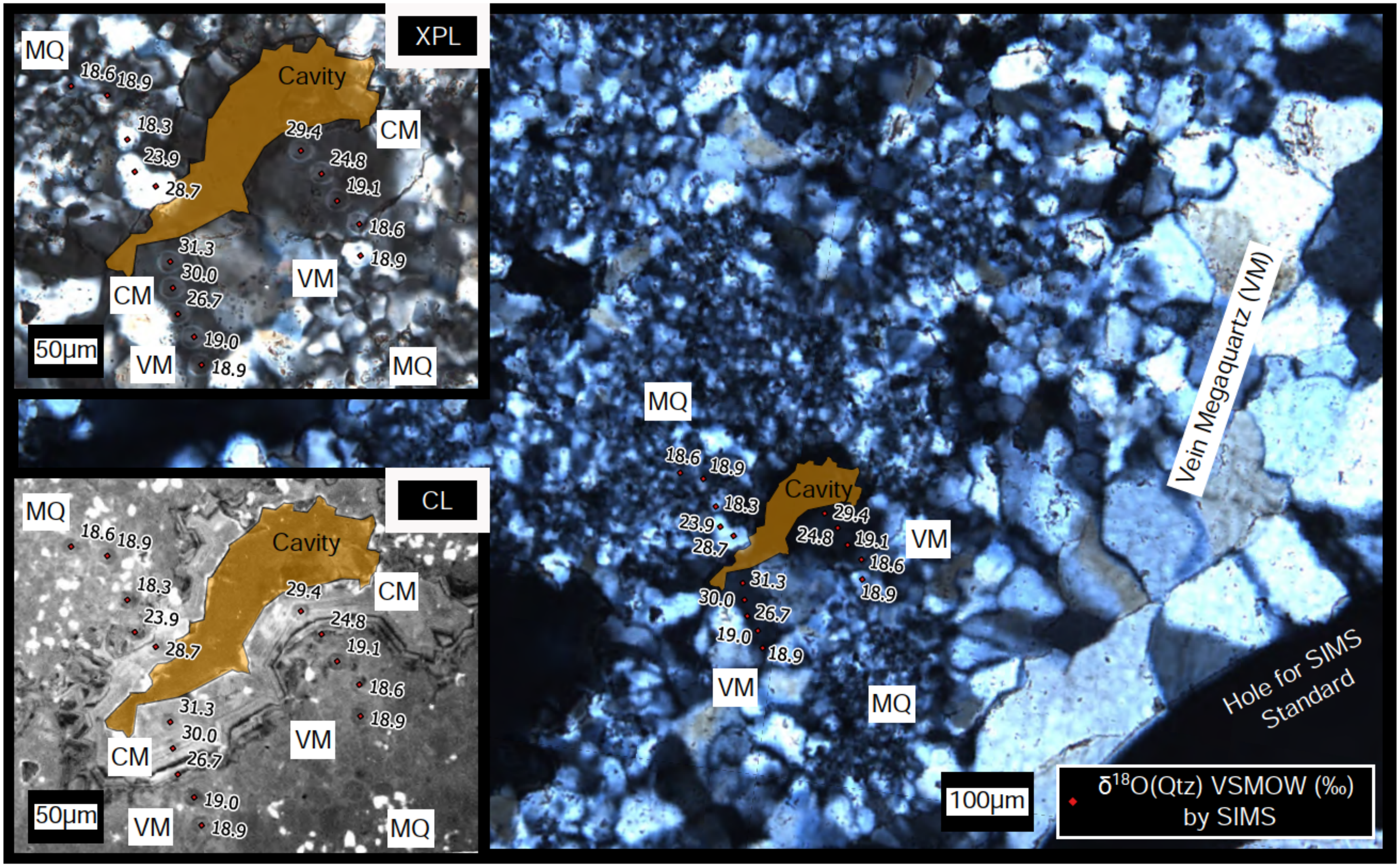

Supplementary Figure 5: Figure text is in a separate document.

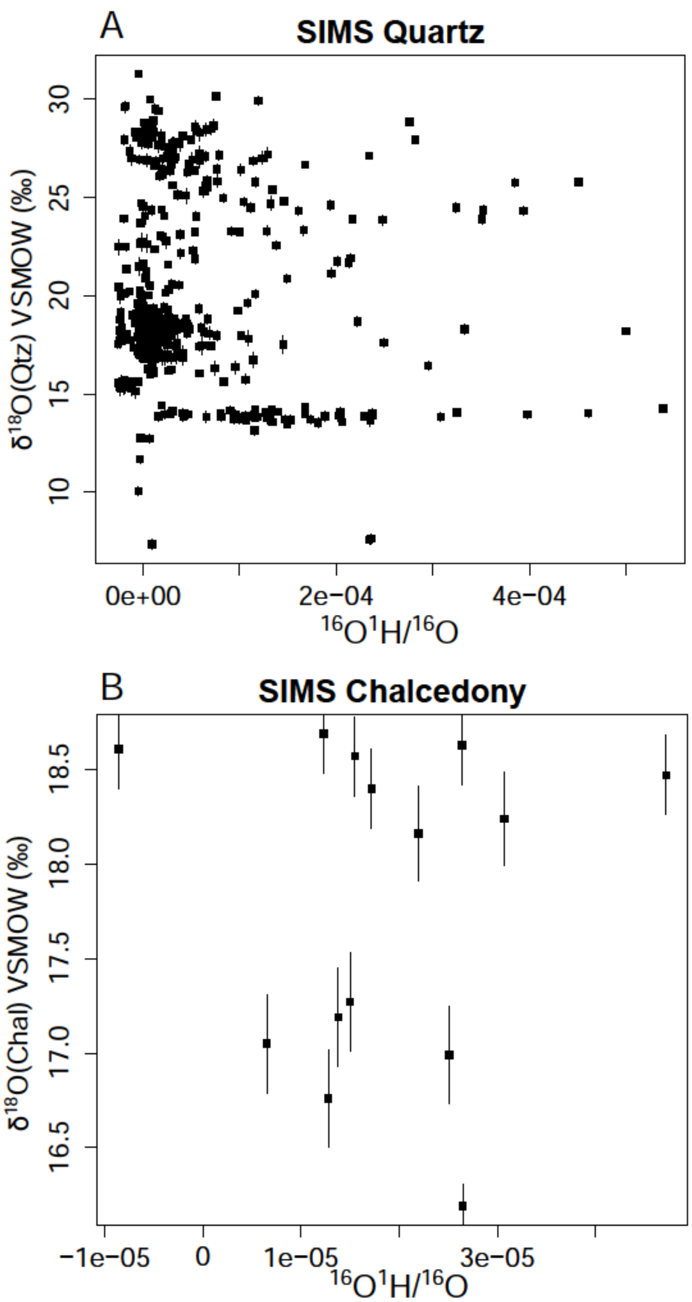

Supplementary Figure 6: Figure text is in a separate document.